Clim Dyn
DOI 10.1007/s00382-008-0441-3

# The global climatology of an interannually varying air–sea flux data set

**W. G. Large · S. G. Yeager**

Received: 25 February 2008 / Accepted: 24 June 2008


**Abstract** The air–sea fluxes of momentum, heat, freshwater and their components have been computed globally from 1948 at frequencies ranging from 6-hourly to monthly. All fluxes are computed over the 23 years from 1984 to 2006, but radiation prior to 1984 and precipitation before 1979 are given only as climatological mean annual cycles. The input data are based on NCEP reanalysis only for the near surface vector wind, temperature, specific humidity and density, and on a variety of satellite based radiation, sea surface temperature, sea-ice concentration and precipitation products. Some of these data are adjusted to agree in the mean with a variety of more reliable satellite and in situ measurements, that themselves are either too short a duration, or too regional in coverage. The major adjustments are a general increase in wind speed, decrease in humidity and reduction in tropical solar radiation. The climatological global mean air–sea heat and freshwater fluxes (1984–2006) then become 2 W/m$^2$ and $-0.1$ mg/m$^2$ per second, respectively, down from 30 W/m$^2$ and 3.4 mg/m$^2$ per second for the unaltered data. However, decadal means vary from 7.3 W/m$^2$ (1977–1986) to $-0.3$ W/m$^2$ (1997–2006). The spatial distributions of climatological fluxes display all the expected features. A comparison of zonally averaged wind stress components across ocean subbasins reveals large differences between available products due both to winds and to the stress calculation. Regional comparisons of the heat and freshwater fluxes reveal an alarming range among alternatives; typically 40 W/m$^2$ and 10 mg/m$^2$ per second, respectively. The implied ocean heat transports are within the uncertainty of estimates from ocean observations in both the Atlantic and Indo-Pacific basins. They show about 2.4 PW of tropical heating, of which 80% is transported to the north, mostly in the Atlantic. There is similar good agreement in freshwater transport at many latitudes in both basins, but neither in the South Atlantic, nor at 35°N.

W. G. Large (✉) · S. G. Yeager
National Center for Atmospheric Research, P.O. Box 3000, Boulder, CO 80307-3000, USA
e-mail: wily@ncar.ucar.edu

## 1 Introduction

There are numerous oceanic, as well as atmospheric and coupled, studies that require knowledge of air–sea fluxes. These needs prompted the formation of a Joint JSC/SCOR Working Group on Air–Sea Fluxes (WGASF). The final report (Taylor 2000) is a comprehensive assessment of most aspects of the subject, but flux variability is a notable exception. However, it does comment on the desirability of examining the variability of the fluxes themselves, rather than of more readily available flux parameters such as sea surface temperature (SST), or winds inferred from sea level pressure (SLP).

In modeling studies where air–sea fluxes are internally computed, the fluxes and their components should be compared to independent estimates as a necessary, though insufficient, test of model performance. This practice should apply to the Atmospheric Modeling Intercomparison Project (AMIP) protocol (Gates 1992), where only SST is specified, to fully coupled atmosphere-ocean models (IPCC 2007), and to ocean modeling when air–sea fluxes are computed from prognostic SST. A variant of the latter would be the coupled ocean-ice Coordinated Ocean Research Experiments (CORE) proposed by the CLIVAR Working Group on Ocean Model Development (Griffies et al. 2008).

Prescribed fluxes have been used as control variables in some attempts to produce an ocean reanalysis (Stammer et al. 2002). In regions of ocean model fidelity (e.g. over subtropical gyres away from western boundary currents), Stammer et al. (2004) conclude that the assimilation of ocean observations leads to flux increments that tend to improve the mean fluxes.

A very important component of the final WGASF report is an evaluation of existing flux products. Those based on in situ data include: COADS (The University of Wisconsin-Milwaukee version of the Cooperative Ocean Atmosphere Data Set) (DaSilva et al. 1994) and NOC1.1 from the National Oceanography Centre, which was originally the Southampton Oceanography Centre (SOC) climatology (Josey et al. 1998). The Hamburg Ocean Atmosphere Parameters and fluxes from Satellites (HOAPS) data set (Jost et al. 2002) is the most complete satellite based product evaluated. Operational analyses were excluded, because numerical weather prediction (NWP) systems frequently change. However, both the NCEP (Kalnay et al. 1996) and ERA15 (Gibson et al. 1997) reanalysis flux products were evaluated. A critical, albeit disappointing, conclusion of the report was that "there is currently no one flux climatology which does not exhibit significant errors in one region or another in each of the various flux components." Nevertheless, studies of the North Atlantic Oscillation, for example, have used fluxes from COADS (Cayan 1992a, b), NOC1.1 (Josey et al. 2001) and NCEP (Visbeck et al. 2003).

Since the WGASF report, there have been a number of notable attempts to improve the state-of-the-art regarding global air–sea fluxes. However, only two include a complete set of global fluxes and flux parameters. One is the 1957–2002 ERA40 reanalysis (Uppala et al. 2005). As with all NWP (re)analyses, products such as radiation and precipitation that depend directly on clouds may not be reliable (Taylor 2000), because cloud observations are not assimilated. The second is the Ocean Model Intercomparison Project (OMIP) data set (Roske 2006), that was constructed as a forcing for ocean general circulation models (OGCMs), but there is no interannual variability, because only mean annual cycles of daily values are given. It is based on the ERA15 reanalyses, but in order to deal with "flaws in the reanalyses", such as the above cloud issues, an inverse procedure (Isemer et al. 1989) was applied to close the data set in terms of global heat and freshwater balance, and a scheme for katabatic winds around Antarctica was introduced. According to Roske (2006), it is unclear if the inversion improves suspect shortwave radiation in the high latitude Southern ocean, subsidence zones and the tropics.

Less complete are the Japanese Ocean Flux data sets with Use of Remote sensing Observations (J-OFURO) (Kubota et al. 2002) that are based primarily on satellite remote sensing. They are not global, except for the latent heat flux, and do not include precipitation, wind direction or air humidity. The common period of overlap of the various J-OFURO flux products is only 1992–1995.

Two other efforts have focused on improving the air–sea heat flux. First, Grist and Josey (2003) present a linear inverse analysis of the NOC1.1 climatology using ten ocean heat flux constraints. Although the global mean net heat flux into the ocean is reduced from 30 to $-5$ W/m$^2$, it is still inconsistent with observed ocean temperature changes that suggest a small positive imbalance (Levitus et al. 2000). Only with the addition of a $\pm 2$ W/m$^2$ global constraint could the criterion of Isemer et al. (1989) be satisfied, but then the global imbalance only rises to the lower limit of the constraint ($-2$ W/m$^2$), and implied transports are systematically near the lower limits of the three transport constraints in the North Atlantic between 8°N and 24°N. The adjusted heat flux data set is distributed as NOC1.1a, but only as a monthly climatology, and without consistently adjusted flux parameters such as winds, air temperatures and humidities. Second, Yu et al. (2004) attempt to improve the heat flux through a variational Objective Analysis (OAflux) approach. The methodology synthesizes atmospheric state variables and SST from satellite retrievals and NWP analyses, but not from COADS ship reports. The products are daily, gridded heat flux components over the global ocean that have been validated against in situ flux measurements from ocean surface buoys. The climatological global average heat flux, at least of an early version, is about 30 W/m$^2$ (L. Yu, personal communication, 2006), which not all flux applications can tolerate. An analysis of the sensible and latent heat fluxes from 1981 to 2005 is presented in Yu and Weller (2007).

The present work utilizes an alternative approach to provide global estimates of all the air–sea fluxes that captures as much interannual variability as possible. In the process, a complete suite of flux parameters has been assembled, which can provide interannually varying forcing for ocean and sea-ice models, including CORE. A requirement of such forcing is sub-daily wind resolution of the inertial period and of storm events. The fluxes are to be independent of ocean transport estimates, as well as self-consistent. Examples of self-consistency are that evaporation remains proportional to latent heat flux, that the downwelling longwave radiation and the solar radiation are calculated together, and that the same winds are used to compute the wind stress, turbulent heat fluxes and evaporation. The products can be continually updated to within a few years of the present as needed data sets are extended in time. They can also be improved as more accurate comparison data become available. Furthermore, radiation and

precipitation from NWP analyses and re-analyses are not to be used in any way.

The fluxes are computed from forcing data sets assembled by Large and Yeager (2004), hereafter LY04. The key to the approach is to reduce known biases, by comparing to more accurate and reliable observations that are either too regional, or too short to be suitable themselves. The fundamental assumption that biases are stationary cannot be completely tested, but should become more sound as the space and time scales of the comparison increases. The primary purpose of the present work is to assess the success of the approach in producing global air–sea fluxes over recent decades. Important metrics are global mean fluxes of heat and freshwater that agree with observed decadal changes in ocean temperature and salinity, and with observational estimates of ocean transports.

The first version of the forcing data contains two options described in LY04. The normal year forcing (NYF) consists of a repeat annual cycle of everything needed to force a coupled ocean sea-ice model. It is the forcing of the CORE I experiments in Griffies et al. (2008) and hence is referred to as CORE-NYF.v1. The interannual forcing option (CORE-IAF.v1) varies from year to year and is used in some experiments of Biastoch et al. (2008) and by Yeager and Large (2004), for example, but only goes through 2000. The air–sea fluxes obtained by using this forcing with observed SST, rather than model prognostic SST, are presented in LY04 and are now referred to as CORE.v1 fluxes.

The second version of the fluxes (CORE.v2) has been extended through 2006 and is the subject of this study. The present focus is more on the global climatology than the variability. The flux calculations are reviewed briefly in Sect. 2, with the formulation of the turbulent transfer coefficients given in the "Appendix". The various data sets are described in Sect. 3, along with all the bias reductions that define the CORE-IAF.v2 and its differences from CORE-IAF.v1. Section 4 presents the resulting mean CORE.v2 flux fields and the implied ocean heat and freshwater transports. Regional average fluxes are compared with available alternatives in Sect. 5. Section 6 shows how the CORE.v2 heat and freshwater fluxes vary from year to year on basin to global scales. Finally, a discussion and concluding remarks follow in Sect. 7.

The ocean-ice model forcing (CORE-NYF.v1, CORE-IAF.v1 and CORE-IAF.v2) plus release notes and support code are freely available at http://nomads.gfdl.noaa.gov (/nomads/forms/mom4/CORE.html). This web site is generously supported by scientists at NOAA's Geophysical Fluid Dynamics Laboratory in collaboration with the National Center for Atmospheric Research (NCAR). A CORE-NYF.v2 has not yet been constructed. The CORE.v2 fluxes are freely available from NCAR's Research Data Archive at http://dss.ucar.edu/datasets/ds260.2.

## 2 Air–sea fluxes

The ocean is forced by the fluxes of freshwater $F$, heat $Q$, and momentum $\vec{\tau}$ (with components $\tau_\lambda$ in the zonal and $\tau_\phi$ in the meridional directions). In general, a fraction of the ocean surface is covered by sea-ice, leaving a fraction, $f_o$, exposed to the atmosphere above:

$$\vec{\tau} = f_o \vec{\tau}_{as} + (1 - f_o)\vec{\tau}_{io} \tag{1a}$$

$$F = f_o F_{as} + (1 - f_o) F_{io} + R \tag{1b}$$

$$Q = f_o Q_{as} + (1 - f_o) Q_{io}, \tag{1c}$$

where the subscripts "as" and "io" denote air–sea and ice–ocean fluxes, respectively. In (1b), $R$ is the total continental runoff, which here is treated as a surface freshwater flux.

Computing ice–ocean fluxes and their variability over decades from observations is not yet a tractable problem, although coupled ocean sea-ice models (Griffies et al. 2008) do produce complete data sets. Fortunately, ice–ocean fluxes are not essential for present purposes and none are computed. In many regions sea-ice is approximately in free drift, so standard calculations (Hunke and Holland 2007) of the wind forcing of the ice are often reasonable estimates of $\vec{\tau}_{io}$. Globally only about 10% of the ocean is covered by sea-ice, and $Q_{io}$ tends to be small (e.g. a few W/m$^2$ cooling over the central Arctic), because sea-ice is an effective insulator. Also, the negative $F_{io}$ in regions and seasons of ice formation, and the positive flux of ice melt are local signals that are important for forcing ocean models, but they tend to cancel over the larger scales of present interest. Therefore, the focus will be on the air–sea forcing, $f_o\vec{\tau}_{as}$, $f_o F_{as}$ and $f_o Q_{as}$.

The air–sea heat and freshwater fluxes are computed by summing estimates of their components:

$$Q_{as} = Q_S + Q_L + Q_E + Q_H \tag{2a}$$

$$F_{as} = P + E, \tag{2b}$$

where all the fluxes are defined to be positive when momentum, water or heat pass into the ocean. The shortwave, or solar radiation, $Q_S$, includes wavelengths between 0.3 and 3 $\mu$. Longer wavelengths, up to 50 $\mu$, comprise the longwave radiation, $Q_L$. The turbulent fluxes are the wind stress, $\vec{\tau}_{as}$, and the sensible $Q_H$, and latent $Q_E$, heat fluxes and evaporation $E$. All precipitation $P$, will be assumed to fall as rain at the same temperature as the SST, so heat fluxes associated with temperature changes and melting snowfall are neglected for present purposes.

Bulk formulae parameterize the turbulent fluxes in terms of the near surface atmospheric state (wind $\vec{U}$, potential

temperature $\theta$, specific humidity q, and density $\rho$) and the ocean state (SST and ocean surface current, $\vec{U}_o$):

$$\vec{\tau}_{as} = \rho C_D |\Delta\vec{U}| \Delta\vec{U} \tag{3a}$$

$$E = \rho C_E (q - q_{sat}(SST)) |\Delta\vec{U}| \tag{3b}$$

$$Q_E = \Lambda_v E \tag{3c}$$

$$Q_H = \rho c_p C_H (\theta - SST) |\Delta\vec{U}|, \tag{3d}$$

where $\Delta\vec{U} = \vec{U} - \vec{U}_o, c_p \approx 1{,}000.5$ J/kg per °C, is the specific heat of air, and $\Lambda_v \approx 2.5 \times 10^6$ J/kg, is the latent heat of vaporization. The air at the ocean surface is assumed to be saturated with its specific humidity approximated by:

$$q_{sat}(SST) = 0.98 \rho^{-1} 640{,}380 (kg/m^3) e^{(-5107.4K/SST)}, \tag{4}$$

where the factor 0.98 applies only over sea-water. The complete methodology, including how the transfer coefficients for drag $C_D$, sensible heat transfer $C_H$, and evaporation $C_E$ are shifted from formulations of their neutral stability values at 10 m height, is detailed in LY04 and also in Large (2006). The formulation of these neutral, 10 m coefficients is documented in the "Appendix".

The radiative flux calculations reduce to functions of SST, the solar insolation $Q_I$, incident on the ocean surface, the solar albedo, $\alpha$, and the downwelling longwave flux from the atmosphere, $Q_A$. The net solar flux is given by

$$Q_S = Q_I (1 - \alpha). \tag{5}$$

The blackbody radiation from the ocean occurs at longer wavelengths and is given by $\varepsilon\sigma(SST)^4$, where $\sigma = 5.67 \times 10^{-8}$ W/m$^2$ per K$^4$ is the Stefan–Boltzmann constant and $\varepsilon$ is the surface emissivity. The net longwave flux becomes

$$Q_L = Q_A - \sigma(SST)^4, \tag{6}$$

where the emissivity is taken to be 1.0 to account for the small fraction of $Q_A$ that is reflected (Lind and Katsaros 1986).

## 3 Data sets and bias reductions

The air–sea flux calculations require the near surface atmospheric state $\{\vec{U}, \theta, q, \rho\}$, downwelling radiation $\{Q_I, Q_A\}$, precipitation, the ocean state $\{SST, \vec{U}_o\}$ and the ice state given by $f_o$. Characteristics of various data sets are given in Table 1. They allow all the air–sea fluxes to be computed through 2006; the turbulent fluxes $\{\vec{\tau}_{as}, E, Q_E, Q_H\}$ from 1948, the radiative fluxes $\{Q_S, Q_L\}$ after 1983 and precipitation from 1979. Therefore, the total air–sea heat $f_o Q_{as}$, and freshwater, $f_o F_{as}$, fluxes are available only after 1983 and from 1979, respectively.

The monthly Hadley Centre sea Ice and SST data set version 1 (HadISST1) is described and evaluated by Rayner et al. (2003). It includes historical SSTs reconstructed from ship observations beginning in 1871 (Folland et al. 2001). It has been merged with version 2 of the National Oceanic and Atmospheric Administration (NOAA) weekly optimum interpolation (OI.v2) analysis (Reynolds et al. 2002) and made compatible with historical sea-ice distributions by Hurrell et al. (2008). Hereafter, this latter product (Hadley-OI) is used exclusively.

Daily fractional sea-ice concentration, $c_i = 1 - f_o$, is estimated from satellite microwave measurements (Comiso 1999) and provided by the National Snow and Ice Data Center (NSIDC). The climatological (1979–2006) distributions of mean concentration are shown for the Arctic in Fig. 1a and the Antarctic in Fig. 1b. Where the mean is zero, ice is not observed and $f_o = 1$ in (1). In the central Arctic (Fig. 1a) and east of the Antarctic Peninsula (Fig. 1b), the air–sea forcing is greatly reduced by mean $c_i > 0.8$. Moving equatorward, there is generally a decrease in this effect to the limits of sea-ice extent at about 47°N and 55°S, but there is an offshore increase in the Ross Sea, because of strong katabatic winds from Antarctica.

### 3.1 The atmospheric state

The atmospheric state is based on NCEP reanalysis from 1949 to 2006, but these data have known biases (Smith et al. 2001) and are, therefore, adjusted based on comparisons with observations. The surface air temperatures are changed only at high latitudes. Around Antarctica a low temperature limit is set, based on weather station and drifting buoy data (F.O. Bryan, personal communication, 2002). This limit and the zonally averaged increases in NCEP $\theta$ in a typical year (1990) are shown as functions of latitude and day of the year in LY04. The coldest limit is −34°C at 77°S in July and the biggest increases are about 12°C during March and April from 75°S to 77°S. Over the Arctic cap north of 70°N, the polar exchange at the sea surface (POLES) air temperatures (Rigor et al. 2000) agree in the climatological mean (−13.83°C vs. −13.93°C for NCEP), but suggest a reduction of NCEP air temperature in spring and summer, and an increase in fall and winter. The 12 monthly adjustments (January–December) are 0.49, 0.06, −0.73, −0.89, −0.77, −1.02, −1.99, −0.91, 1.72, 2.30, 1.81 and 1.06°C.

QSCAT satellite scatterometer wind vectors, $(U_Q, V_Q)$, from the method of Chin et al. (1998) are suitably flagged for rain and best represent a spatial average of $\Delta\vec{U}$. Their accuracy relative to time averaged surface buoy winds is about 1 m/s in speed and 20° in direction for winds less than 20 m/s (Ebuchi et al. 2002; Freilich and Vanhoff 2006). Therefore, comparisons with coincident 6-hourly

**Table 1** Characteristics of datasets used for computing the CORE.v2 fluxes and for determining objective adjustments to forcing data

| Variables | Source | Frequency | Duration | Resolution | Coverage | Basis |
|---|---|---|---|---|---|---|
| SST | Hadley-OI | Monthly | 1871–2007[a] | 1° | Global | Satellite |
| Atmospheric State | NCEP | 6 hourly | 1948–2006[a] | T62 | Global | NWP |
| Radiation | ISCCP-FD | Daily | 1984–2006[a] | 2.5° | Global | Satellite |
| Precipitation | GPCP | Monthly | 1979–2006[a] | 2.5° | Global | Satellite |
| Precipitation | CMAP | Monthly | 1979–2006[a] | 2.5° | Global | Blend |
| Precipitation | S-H-Y | Monthly | Climatology | 0.5° | 50°N–90°N | In situ |
| Ice fraction | NSIDC | Daily | 10/79–2006[a] | 25 km | Global | Satellite |
| All | NOC | Monthly | 1980–1995 | 1° | Global | Ships |
| All | TAO | Daily | 1995–2004[a] | 2°–20° | Pacific | Buoys |
| Most | PIRATA | Daily | 1998–2004[a] | 2°–20° | Atlantic | Buoys |
| Vector winds | QSCAT | 6 hourly | 1999–2004[a] | 0.5° | Global | Satellite |
| Air temperature | POLES | 12 hourly | 1979–2003 | 100 km | 60°N–90°N | In situ |
| Precipitation | MSU | Monthly | 1979–1993 | 2.5° | 55°S–55°N | Satellite |

[a] Ongoing production of the dataset is expected beyond these durations

NCEP vector winds, ($U_N$, $V_N$), yield what can be regarded as corrections to NCEP wind speeds, and adjustments to the wind direction. The modified wind vector ($U$, $V$) is used as $\Delta\vec{U}$ in (3) and is given by a multiplicative factor, $R_S$, applied to the speed plus a rotation by $\delta$ of the NCEP vector.

Figure 2 shows the spatial distributions of $R_S$ and $\delta$, as defined by

$$R_S(\lambda,\phi) = \left\langle (U_Q^2 + V_Q^2)^{\frac{1}{2}} \right\rangle / \left\langle (U_N^2 + V_N^2)^{\frac{1}{2}} \right\rangle \tag{7a}$$

$$\delta(\lambda,\phi) = f(S_N)\left[\tan^{-1}\left(\frac{\langle V_Q\rangle}{\langle U_Q\rangle}\right) - \tan^{-1}\left(\frac{\langle V_N\rangle}{\langle U_N\rangle}\right)\right], \tag{7b}$$

where $\langle\ \rangle$ denotes averages over the 5-year QSCAT period (2000–2004) and $S_N$ is the magnitude of the vector average NCEP wind over this period. The main consideration is to match the mean wind speed from QSCAT (7a) everywhere, because speed enters into all the turbulent flux calculations (3), and the QSCAT speed measurement is direct and well calibrated. The wind speed is increased almost everywhere (reddish regions of Fig. 2a). The largest values of $R_S$ are in the Barents Sea (up to 1.7), over the Southern Ocean (up to 1.40), around the Maritime Continent (up to 1.5) and at about 6°N in the eastern regions of both the Atlantic (up to 1.45) and Pacific (up to 1.65). From (3), the fluxes E, $Q_E$ and $Q_H$ all change by about the same factors, while the respective wind stresses should increase by factors of at least 2.9, 2.0, 2.3, 2.1 and 2.7.

Wind rotations are not applied in LY04 and are still only crude, because the scatterometer wind direction determination is not straightforward and has ambiguities (Naderi et al. 1991). In general, wind direction spans 360°, so associated problems (e.g. the average of 5° and 355° is 0° not 180°) are avoided in (7b) by finding the unique, unambiguous angles defined by wind component means. In order to accommodate low wind regions, especially the transitions between easterlies and westerlies along about 65°S, 30°S and 30°N, the term $f(S_N)$ in (6b) is set to zero (no rotation) for $S_N \leq 2$ , then increases linearly to a maximum of 1 at $S_N \geq 3$ m/s. Over large fractions of other regions, Fig. 2b shows that the NCEP and QSCAT wind directions are in good agreement, with $\delta$ between ±5°. There are significant rotations in the central tropical Pacific, where they produce more cross-equatorial flow and convergence, as well as east of Drake Passage. Otherwise, regions of large rotations ($\delta > 20°$) are mainly confined to near coastal regions, especially along the Pacific coast of South America. These rotations, as well as smaller, systematic rotations applied over large areas of the North Pacific, North Atlantic and Southern oceans, all improve the agreement with the NOC and COADS ship based wind climatologies (see also Sect. 5).

A potentially more accurate procedure for altering NCEP winds using absolute QSCAT wind was explored, but not adopted because the effects on Fig. 2b were small, and because of the QSCAT direction issues. These absolute winds were just the vector sum of the QSCAT winds plus the near surface current from a 1° surface drifter climatology (Hansen and Poulain 1996). Along the equator, they are more zonal, as expected from persistent cross-equatorial easterly winds and westward surface currents, but by less than 6°. Consistent with currents tending to align with the wind direction, absolute speeds were greater than QSCAT, but by less than 2%.

LY04 apply a latitude dependent decrease to the NCEP relative humidity, where the 3% tropical reduction is based on the Wang and McPhaden (2001) comparison with measurements from the Tropical Ocean–Atmosphere

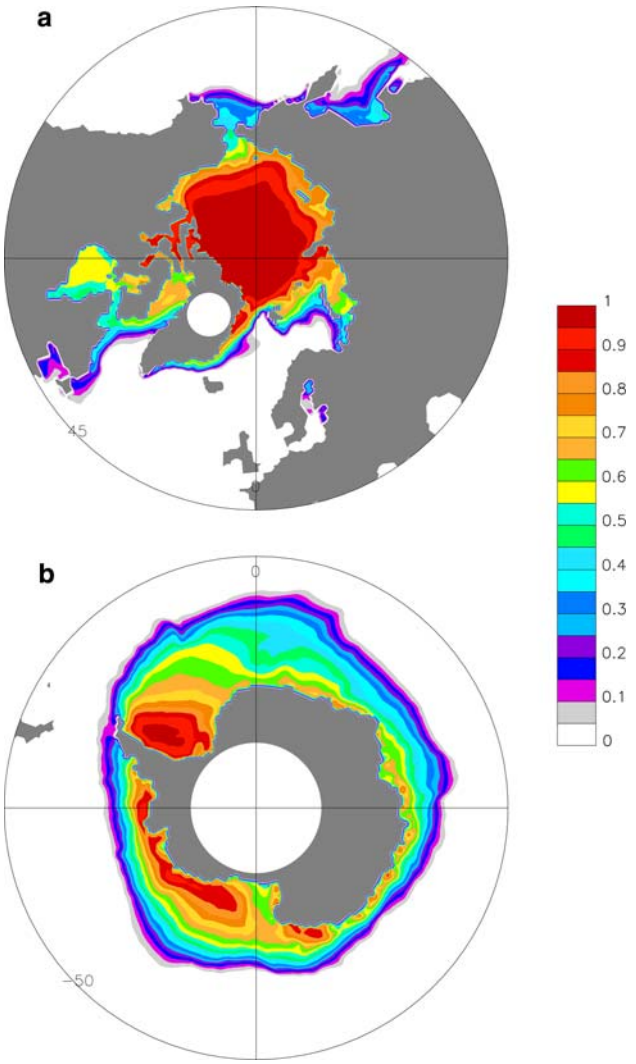


**Fig. 1** Distributions of climatological (1979–2006) fractional sea-ice concentration: **a** over Northern Hemisphere Arctic poleward of 45°N and **b** over the Southern Hemisphere Antarctic poleward of 50°S

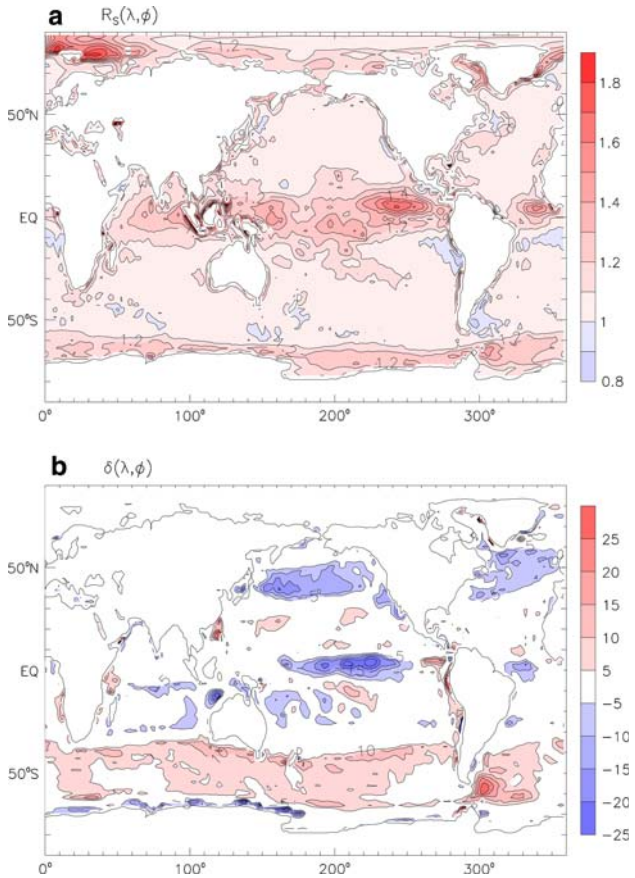


**Fig. 2** Global distributions of the multiplicative speed factor $R_S$, and rotation $\delta$, applied to NCEP wind vectors. **a** $R_S(\lambda, \phi)$ colored at 0.1 intervals, with regions of $R_S > 1$ in red and less than 1 in blue. **b** $\delta(\lambda,\phi)$ colored at 5° intervals, with reds indicating positive (counter-clockwise) rotation by more than 5°, and blues $\delta < -5°$

(TAO) moorings in the tropical Pacific (McPhaden et al. 1998). In contrast, a more recent comparison of TAO specific humidity (Jiang et al. 2005) suggests that NCEP humidity is too low over much of the region. At least some of the discrepancy between the two results likely arises from air temperature differences that are involved in relating specific and relative humidity. Therefore, NCEP specific humidity, the more relevant quantity; namely $q$ in (3b), is now modified. The time invariant adjustment, $\delta q(\lambda,\phi)$, is shown spatially smoothed in Fig. 3. It is just the climatological difference between NOC1.1 and NCEP specific humidities, and is consistent with Jiang et al. (2005) and Smith et al. (2001).

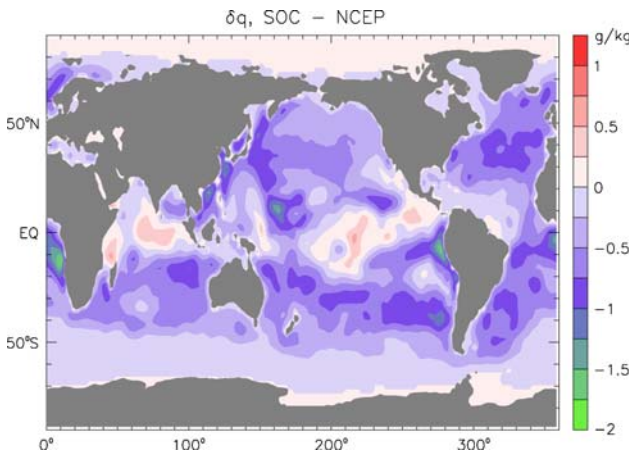


**Fig. 3** Global distribution of the adjustments applied to NCEP specific humidity; after spatial smoothing and colored at 0.25 g/kg intervals

### 3.2 Radiation

The ISCCP-FD data (Zhang et al. 2004) include companion estimates of both $Q_I$ and $Q_A$ from mid-1983 to 2006. Thus, cloud effects in one may be at least partially compensated in the other. The reflected solar radiation is also given, but difficult to use because of contributions from land and sea-ice in many grid cells. Nonetheless, it can be used to determine an effective ocean albedo. The daily insolation and reflected radiation are time averaged over 21 years (1984–2004), then zonally averaged over the ice-free, open ocean. The ratio of these averages gives the latitude dependent albedo shown in Fig. 4 (thin trace). The effective ocean albedo, $\alpha$ used in (5), is given as a function of latitude, $\phi$, by the simple fit (thick curve of Fig. 4):

$$\alpha(\phi) = 0.069 - 0.011\cos(2\phi). \quad (8)$$

Both albedo curves in Fig. 4 agree with the observations of Payne (1972) at 43°N. They give net solar fluxes from (5) that differ by less than 1 W/m$^2$ at all latitudes, and because of compensation they give almost the same average reflected solar over the ice free, open ocean (12.5 W/m$^2$).

The ISCCP-FD insolation is uniformly reduced by 5% between 50°S and 30°N. For smoothness the reduction is linearly diminished to become zero poleward of 60°S and of 40°N. Some reduction is supported by comparisons with the Baseline Surface Radiation Network (Zhang et al. 2004), and with zonal means from other products shown in Beranger et al. (1999) and Taylor (2000). However, before any changes were adopted, differences between the reduced $Q_I$, and measurements from both TAO and PIRATA (Pilot Research moored Array in the Tropical Atlantic) (Servain et al. 1998) buoys were examined. Table 2 shows that over the whole tropical Pacific and Atlantic the remaining biases are not systematic and average only 1 W/m$^2$, though no weights have been applied for factors such as length of record. Despite the 5% ($\approx$10 W/m$^2$) reduction, there are still large regional positive biases (e.g the eastern and northern equatorial Atlantic), that are offset by negative biases across the equatorial Pacific. In principle, these biases could be reduced with full spatial variations in the adjustment, but this could not be done globally, and the issue of stationarity in time would become a greater concern. The ISCCP-FD and J-OFURO fields of $Q_I$ are not dissimilar, so Table 2 suggests that the validation of the latter using land stations mostly in Japan and Australia (Kubota et al. 2002) could benefit from including tropical buoy measurements.

The bracketed values along 265°E (95°W) in Table 2 reveal a tendency for $Q_A$ to be larger in ISCCP-FD than from TAO buoys, but by less than 3 W/m$^2$ in the mean. This difference is less than 1% of a typical 400 W/m$^2$ flux, and not large compared to the measurement accuracy.

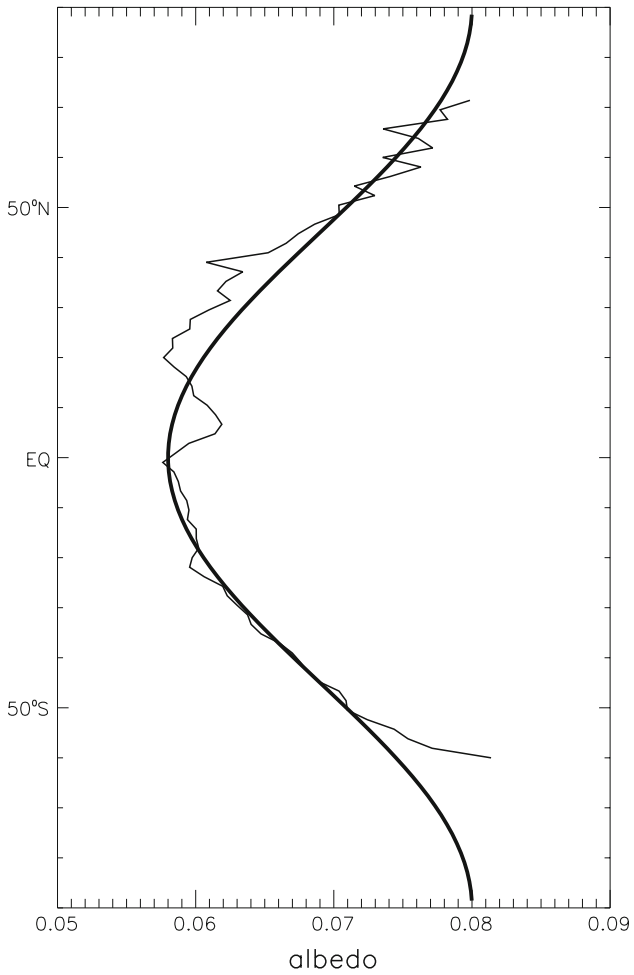


**Fig. 4** Ocean surface solar albedo $\alpha$, as a function of latitude from zonal averages of ISCCP-FD surface radiation from 1984 to 2004 (*thin trace*), and the fit given by Eq. 8 (*thick trace*)

Therefore, $Q_A$ from ISCCP-FD remains unchanged everywhere over the ocean south of 60°N. Farther north there is a linear blend to a 5 W/m$^2$ reduction poleward of 70°N, as suggested by Surface HEat Budget of the Arctic (SHEBA) observations (M. Holland, personal communication, 2008).

### 3.3 Precipitation

Either the Climate Prediction Center Merged Analysis of Precipitation (CMAP) product (Xie and Arkin 1996), or the Global Precipitation Climatology Project (GPCP) data (Huffman et al. 1997) could be suitable for providing long, global records of precipitation (Table 1). Potentially the NOC1.1 climatology and Microwave Sounding Unit (MSU) product (Spencer 1993) could provide verification. Unfortunately, all these data sets differ substantially from each other and there are regions where each appears to be an outlier compared to the others.

**Table 2** Spatial distribution of remaining differences in the adjusted ISCCP-FD radiation (W/m$^2$) relative to TAO buoys in the Pacific, and PIRATA buoys in the Atlantic

| | 156°E | 165°E | 190°E | 220°E | 235°E | 250°E | 265°E | 38°W | 23°W | 10°W | 0°W |
|---|---|---|---|---|---|---|---|---|---|---|---|
| 15°N | | | | | | | | 8 | | | |
| 12°N | | | | | | | | 10 | | | |
| 8°N | | 1 | | | | 11 | 6 (7) | | | | |
| 4°N–5°N | | 5 | | | | | 11 (−2) | 7 | | | |
| 2°N | | −3 | | −11 | | | 7 (4) | | | | |
| EQ | −1 | −4 | −8 | −4 | −4 | −6 | −5 (6) | −3 | 0 | 11 | 18 |
| 2°S | | −2 | | | | | −9 (2) | | | | |
| 5°S–6°S | | 2 | | | | | 1 (1) | | | 1 | |
| 8°S | | 3 | | | | | −5 (1) | | | | |
| 10°S | | | | | | | | | | −4 | |

Only buoys with at least 1 year of data between 1995 and 2004 are included and ISCCP-FD data are sampled to match the monthly buoy averages. Bracketed values along 265°E (95°W) are for downwelling longwave, $Q_A$, while all others are shortwave insolation, $Q_I$. The entry at 0°N 38°W is actually from 35°W. All ISCCP-FD data have been interpolated to buoy latitudes, but not longitudes

This problematic state of affairs is clearly evident in Fig. 5, which shows the zonal means of these four products, averaged over their common years (1980–1993), even though the zonal averaging obscures larger regional discrepancies. There is a degree of consistency only around 30° latitude in both hemispheres. Therefore, a choice was made for each of five zones; the Antarctic (poleward of 65°S), the Southern (65°S–30°S), the Equatorial (30°S–30°N), the Northern (30°N–70°N) and the Arctic. In the Equatorial zone GPCP is preferred, because CMAP is an outlier and at least some ocean models are unable to cope with so much rainfall in the western Pacific (Large and Danabasoglu 2006; Yeager et al. 2005).

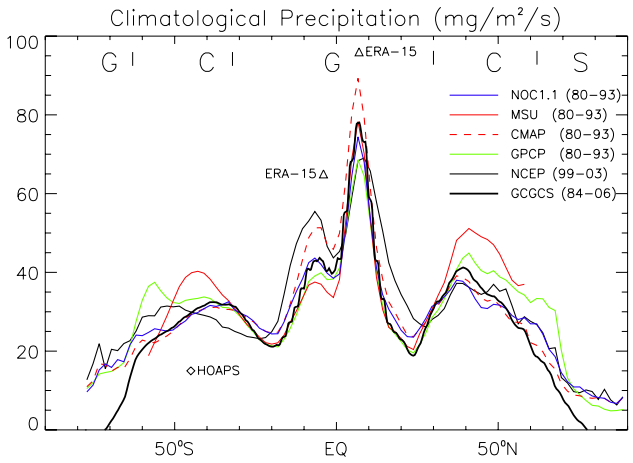


**Fig. 5** Meridional distributions of zonally averaged precipitation from various sources described in the text, mostly over the common years 1980–1993, except for NCEP (1999–2003) and the combined GCGCS product (1984–2006). For clarity, climatological values from ERA-15 and HOAPS are shown only at a few discrete latitudes. Units are mg/m$^2$ per second (0.084 mm/day = 3.1 cm/year)

CMAP is chosen for the Northern zone, because of its general agreement with the independent NOC1.1 climatology where its sampling is best, and in the Southern, mainly because GPCP becomes an outlier, with the NOC1.1 agreement given less weight because of sampling issues. In practice, the CMAP and GPCP data are linearly blended between 25° and 35° latitude.

The merged CMAP product appears to become dominated at high latitudes by model (NCEP) precipitation, because both display spatial patterns associated with the spectral model topography extending away from Greenland and the Antarctic Peninsula. In the Antarctic a simple practical alternative is to blend back into GPCP between 65°S and 60°S. In the Arctic it seems preferable to use the combined Serreze and Hurst (2000) and Yang (1999) (S–H–Y) climatology, with a linear blend to CMAP between 65°N and 70°N. The lack of variability is not a major concern, because of the small ocean area involved.

The most distinctive and important precipitation feature in Fig. 5 is the peak at about 8°N. With the above combination of data sets this peak is smaller than NOC1.1, MSU and CMAP, so it is made equal to the average (1980–1993) of all four data sets by multiplying all satellite precipitation (GPCP and CMAP) by a constant factor of 1.14 before blending with S–H–Y. Hereafter, the resulting product is used exclusively and referred to as GCGCS to reflect the data sources from south to north (GPCP, CMAP, GPCP, CMAP and S–H–Y). The climatological (1984–2006) zonal average $f_o P$ is plotted in Fig. 5, from which it can be inferred that over this period precipitation was stronger in the tropics and weaker at southern mid-latitudes than between 1980 and 1993. The agreement with NOC1.1 between 50°N and 50°S is good, considering the different

years. Only GCGCS is multiplied by $f_o$, so it rapidly decreases at higher latitudes, where the other data sets include precipitation onto sea-ice (Fig. 1).

Figure 5 also serves to illustrate why NCEP precipitation is not considered for the freshwater flux calculation. It is an outlier over many southern latitudes, as well as between 10°N and 25°N. It also appears to be give far too much rainfall between about 15°S and the equator. This feature is likely related to a tendency for atmospheric models to develop a "double" ITCZ in the south Pacific, and appears to a lesser extent in the blended CMAP product. Although ERA15 precipitation is only shown at two latitudes to reduce clutter in Fig. 5, it is apparent that this double ITCZ problem is more acute in ERA15, and that there is excessive rainfall in the northern ITCZ zones too. The single zonal average from HOAPS at 45°S in Fig. 5 demonstrates why this data set was not considered to be an option.

## 4 Climatological air–sea fluxes

This section examines the CORE.v2 climatological air–sea fluxes, which here refers to averages over the 23 years (1984–2006) of complete data coverage (Table 1). First, the global balances of the heat and freshwater fluxes are presented. Second, global maps of the climatological air–sea fluxes and their components are shown, followed by the ocean transports of heat and freshwater implied by these fluxes. Finally, zonal and regional average fluxes are compared to several available alternatives.

Hereafter, the freshwater flux unit of 1 mg/m$^2$ per second ($\approx$0.0864 mm/day $\approx$3.1 cm/year) is used, because at 5°C it contributes approximately the same ocean density flux as the heat flux unit of 1 W/m$^2$ (Large and Nurser 2001). Also from (3c), multiplying evaporation in this unit by a factor 2.5 conveniently gives latent heat flux in W/m$^2$.

### 4.1 Global heat and freshwater balances

Arguably, the most well known flux constraints are that the global long-term heat and freshwater fluxes into the ocean should both be near zero. With the sun as a heat source and space as a sink, the global ocean temperature could be changing rapidly, but Levitus et al. (2000) find that the temperature of the world's oceans above 3,000 m increased from 950s to 1990s at a rate equivalent to a surface heat flux imbalance of only 0.3 W/m$^2$. There is no external source of water, so a global freshwater flux imbalance must be accompanied by variations in land storage (e.g. lakes, aquifers, glaciers and ice sheets). However, observed changes in ocean salinity show that the imbalance has been negligible relative to the typical 10 mg/m$^2$ per second scatter in Fig. 5. For example, even the relatively large decade salinity change reported by Curry and Mauritzen (2005) in the northern North Atlantic corresponds to only 2,000 km$^3$/year of freshwater, or a global flux of only about 0.2 mg/m$^2$ per second.

Table 3 shows that with none of the Sect. 3 adjustments the global average, climatological heat flux would be much too high at 30 W/m$^2$. Individually, the increase in wind speed, the generally lower specific humidity, and reduced solar radiation, respectively decrease this imbalance by 10, 11 and 8 W/m$^2$. In combination, the largest overall change is the 19 W/m$^2$ greater cooling by the latent heat flux, and the imbalance over the 23 years becomes about 2 W/m$^2$. The ocean surface heat flux (1) should be less by order 1 W/m$^2$, and hence more consistent with Levitus et al. (2000), because of heat loss through the sea-ice and the cooling effects of precipitation, runoff and icebergs.

Table 3 also quantifies how the near-zero net CORE.v2 global heat flux is achieved through a balance of large heating terms with large cooling terms. The largest global heating (not shown) is the roughly 360 W/m$^2$ downwelling longwave radiation, $Q_A$, which ranges from nearly 400 W/m$^2$ in the tropics to about 300 W/m$^2$ at polar latitudes. The other significant heating (165 W/m$^2$) is the net shortwave flux. The longwave surface blackbody emission from the ocean is by far the largest cooling term (−400 W/m$^2$). Globally, it more than compensates $Q_A$, by about −53 W/m$^2$ = $Q_L$ (Table 3). The remainder of the global air–sea cooling comes from the turbulent sensible and latent heat fluxes, with the latter about seven times more negative than the former. In general a similar balance holds for individual basins. However, at high latitudes there is a net cooling that increases with latitude as the shortwave heating declines. Factors that reduce this cooling trend are the more balanced

**Table 3** Global mean air–sea fluxes over 23 years (1984–2006), and climatological continental runoff, $R$, from unaltered data, with the wind speed correction only, with the specific humidity adjustment only and with all CORE.v2 adjustments

| | Adjustments | | | |
|---|---|---|---|---|
| | None | Wind | Humidity | All |
| $f_oQ_S$ | 173 | 173 | 173 | 165 |
| $f_oQ_L$ | −53 | −53 | −53 | −53 |
| $f_oQ_E$ | −77 | −85 | −87 | −96 |
| $f_oQ_H$ | −13 | −14 | −13 | −14 |
| $f_oQ_{as}$ | 30 | 20 | 19 | 2 |
| $f_oE$ | −30.6 | −33.8 | −34.9 | −38.4 |
| $f_oP$ | 30.6 | 30.6 | 30.6 | 34.9 |
| R | 3.5 | 3.5 | 3.5 | 3.5 |
| $f_oF_{as} + R$ | 3.5 | 0.2 | −0.9 | −0.1 |

Heat fluxes are in W/m$^2$, and freshwater fluxes are in mg/m$^2$ per second (0.0864 mm/day $\approx$ 3.1 cm/year)

longwave components and the much reduced latent heat flux loss.

The global freshwater budget in Table 3 must necessarily include the continental runoff from rivers, groundwater and icebergs. This runoff has been estimated from continental imbalances between precipitation, evaporation and storage (e.g. Baumgartner and Reichel 1975), then partitioned among bordering ocean basins, using river routing schemes and flow estimates (Fekete et al. 1999). The climatological global average is $1.26 \times 10^9$ kg/s $= 1.26$ Sv (LY04), which gives $R = 3.5$ mg/m$^2$ per second. The difference from the Dai and Trenberth (2002) value of 1.18 Sv is largely due to including about 0.07 Sv of runoff from Antarctica.

According to Table 3, the unaltered data give too much freshwater entering the ocean. The increase in evaporation due to the wind speed and humidity adjustments reduce this by 3.2 and 4.3 mg/m$^2$ per second, respectively. There is then too little freshwater flux, that cannot be accounted for by increasing the runoff, because the data are more accurate than the factor of 2 required. However, the factor 1.14 multiplication of satellite based precipitation results in a global freshwater imbalance of only about $-0.1$ mg/m$^2$ per second, that does not include precipitation falling on sea-ice before reaching the ocean.

### 4.2 Spatial distributions

The climatological CORE.v2 zonal and meridional wind stress components are shown in Fig. 6. The asymmetry across the equator in both components is prominent in all basins and reflects the distribution of the continents. The change in sign of the zonal stress across the equator is unique to the Indian Ocean. The details in the Atlantic and Pacific are influenced by greater cross-equatorial flow resulting from the wind rotation and north of the equator the increase in wind speed more than doubles the stress magnitude in some areas. Nevertheless, the stress patterns are smooth and the spatial variability of changes made to the NCEP winds (Fig. 2) is obscure.

Prominent features of the wind stress are the small scale near coastal jets. The strength of the southward stress to the west of Greenland is enhanced by more than 50% by the wind speed increase, as is the southwestward stress over the Denmark Strait. Equatorward mean meridional stress is found off the west coasts of North and South America, Australia, Southwest Africa and North Africa. The precise strength and direction of these upwelling favorable winds is very important to ocean dynamics and heat budgets in these regions, and have been considerably improved by the changes to the NCEP winds (Fig. 2). The Somali jet off the Horn of Africa is little changed from NCEP and persists in the

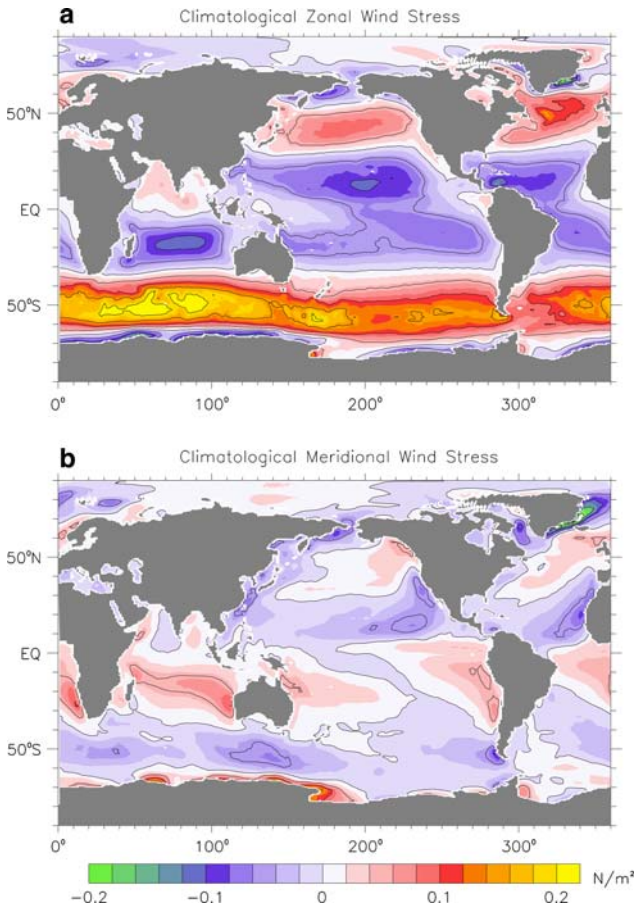


**Fig. 6** Global distributions of the climatological CORE.v2 air–sea momentum flux components: **a** zonal, with eastward wind stress on the ocean positive, **b** meridional, with northward stress positive. Colored at 0.02 N/m$^2$ intervals, with 0.05 N/m$^2$ contour intervals

climatological means of both components, but would be better examined as a seasonal cycle.

Figure 7 shows the global distribution of climatological freshwater flux ($f_o F_{as}$), plus the precipitation and evaporation components. Some features that depend on the precipitation may not be familiar, because of the spread in available estimates (Fig. 5). The obvious freshwater source regions are the intertropical convergence zones (ITCZs) and the midlatitude storm tracks of both hemispheres where precipitation (Fig. 7b) dominates evaporation (Fig. 7c). The opposite (net water loss) holds in the strong evaporation regions of the Arabian Sea and the subtropical gyres of each ocean basin. It is greatest in the Red Sea, Persian Gulf and Gulf of Aden where precipitation is near zero and evaporation very strong. The warm SSTs associated with western boundary currents are reflected in Fig. 7c as extrema in $E$, but these features tend to be canceled in $F_{as}$ by storm track precipitation. The eastern tropical Pacific is notable for the small scale variability in Fig. 7a arising from the proximity of strong ITCZ precipitation

(Fig. 7b), subtropical evaporation, and the weak evaporation associated with the equatorial cold tongue (Fig. 7c).

There is a close correspondence between tropical precipitation and wind stress convergence. Although there should be such a relationship, it is not guaranteed, because of the independent data. The precipitation maxima in the Atlantic and eastern Pacific are related to convergence of meridional stress, whereas in the western Pacific it is the zonal stress that matters most. The reduced precipitation farther north off West Africa is consistent with the cancellation of meridional convergence by zonal stress divergence in Fig. 6.

The CORE.v2 climatological mean air–sea heat flux ($f_o Q_{as}$) is shown in Fig. 8. All the expected features are evident, but their magnitudes may differ from unbalanced, or constrained climatologies. The near-zero global balance is attained through an area weighted cancellation of strong heating with strong cooling. The upwelling of colder water from depth leads to strong heating along the equator with a maximum of about 150 W/m$^2$ in the east Pacific cold tongue, and along the eastern boundaries of the Pacific and Atlantic subtropical gyres. Poleward circulation of warm surface water results in strong cooling of the Nordic seas ($-Q_{as} > 100$ W/m$^2$), the Labrador Sea and the western boundary currents ($-Q_{as} > 180$ W/m$^2$) and their extensions, including the Agulhas retroflection ($-Q_{as} > 120$ W/m$^2$).

The solar, longwave, and sensible, heat flux climatologies are shown in Fig. 9. The distribution of latent heat flux can easily be inferred from the evaporation of Fig. 7c, because from (3c), the 10 mg/m$^2$ per second contour interval corresponds to a latent heat flux of 25 W/m$^2$. Over most of the ocean the net heat flux (Fig. 8) is a balance between solar heating and cooling due to $Q_E$ plus $Q_L$. However, the sensible heat flux, $f_0 Q_H$ is a significant contribution to the cooling where strong winds blow very cold continental air over western boundary currents and their extensions, the Nordic and Labrador seas and the marginal ice-zones. The relatively small cooling by a latent heat flux of between −50 and −75 W/m$^2$ (Fig. 7c) is a major factor in the net heating (Fig. 8) of both the eastern equatorial Pacific, and along the eastern boundaries of the South Atlantic and South Pacific. Another influence along these boundaries is the relatively small cooling by a longwave flux of only about −30 W/m$^2$.

The band of predominant heating in the south Atlantic and Indian Oceans along 50°S appears to reflect topographic steering, especially east of Drake Passage, of cold polar waters to the north and underneath a more temperate atmosphere. This band is aligned with relative minima in

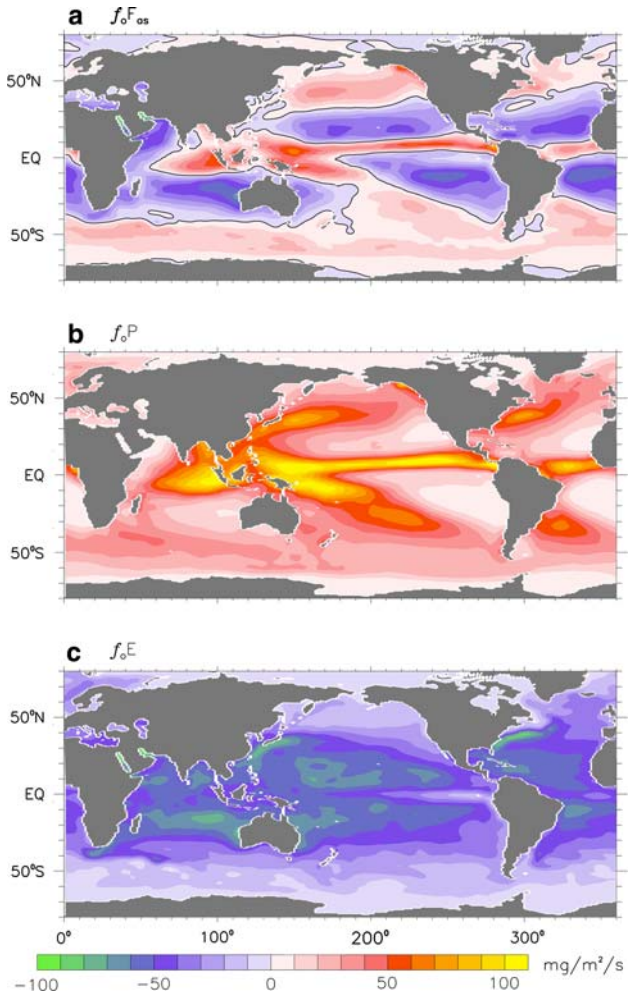


**Fig. 7** Global distributions of the climatological CORE.v2 air–sea fluxes of **a** freshwater, **b** precipitation, **c** evaporation, colored at 10 mg/m$^2$ per second intervals with a zero contour. Multiplication of the evaporation by a factor of 2.5 gives the latent heat flux in W/m$^2$

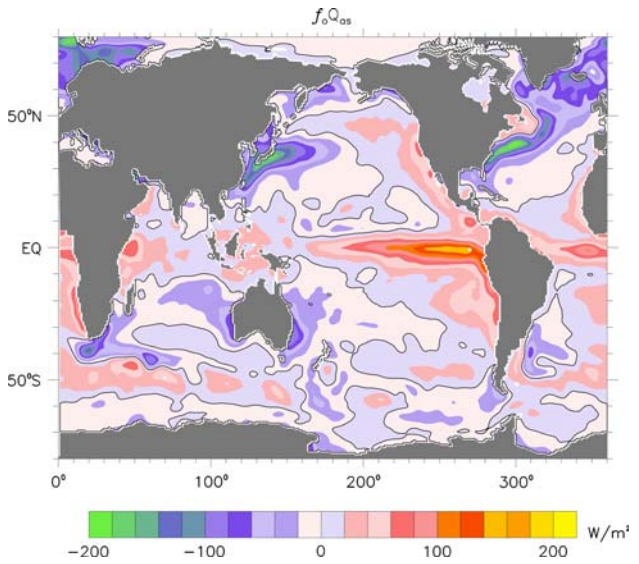


**Fig. 8** Global distribution of the climatological CORE.v2 net air–sea heat flux. The coloring is at 20 W/m$^2$ intervals, with positive values where the heat flux is into the ocean

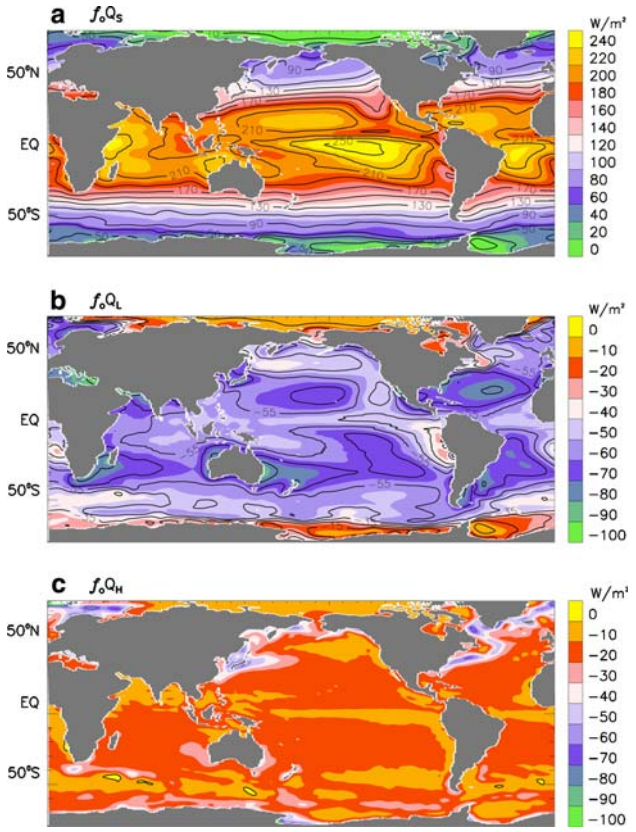


**Fig. 9** Global distributions of the climatological CORE.v2 air–sea heat flux components: **a** net solar radiation, with 20 W/m$^2$ contour intervals; **b** net longwave radiation, with 10 W/m$^2$ contour intervals; **c** sensible heat flux, with coloring at 10 W/m$^2$ intervals. The latent heat flux can be inferred by multiplying the evaporation of Fig. 7c by a factor of 2.5

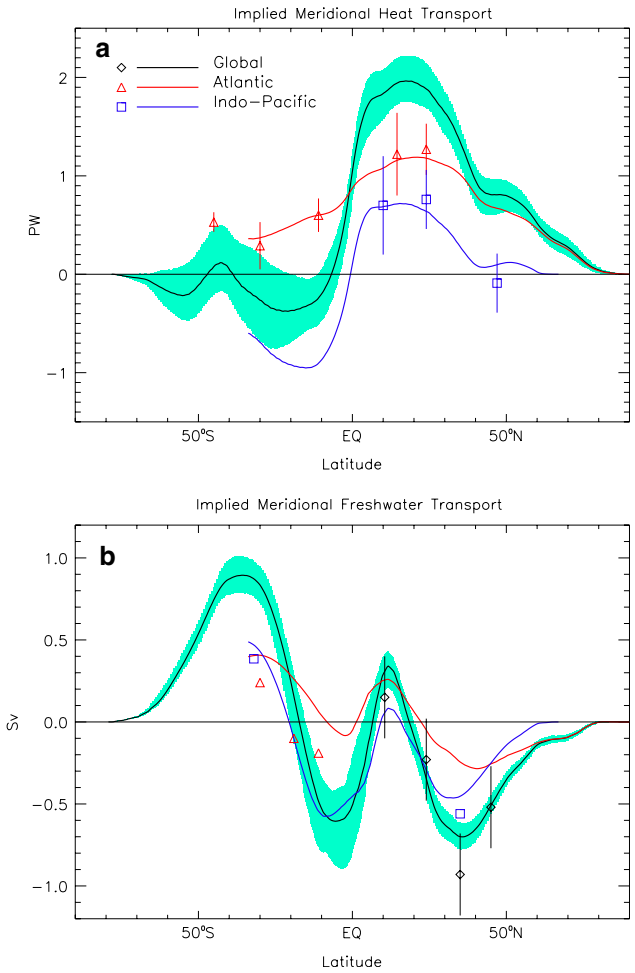


**Fig. 10** Northward ocean transports of **a** heat in PW, **b** freshwater in Sv. Implied transports from the climatological CORE.v2 air–sea heat and freshwater fluxes plus runoff are shown by the *black*, *red* and *blue* traces for the global ocean, the Atlantic Ocean and the Indo-Pacific basin, respectively. The range of the global implied transports in individual years is indicated by the *shading*. Direct estimates from ocean hydrographic sections across entire basins are shown as *diamonds*, *triangles* and *squares*, again for the global ocean, the Atlantic Ocean and the Indo-Pacific basin, respectively

cooling by the sensible heat flux (Fig. 9c) and to lesser extent the latent heat flux (Fig. 7c), as would be expected, but longwave radiation (Fig. 9b) also plays a part. The latter suggests that the cloud fields may be a contributing factor in this net heating.

### 4.3 Implied ocean transports

The climatological air–sea fluxes plus continental runoff imply mean northward ocean transports of heat and freshwater; subject to assumptions regarding flux biases and ocean storage. Although bias and storage effects cannot be separated with the data at hand, different assumptions can be checked for consistency with transports estimated from ocean observations. Figure 10a shows the heat transports across the Atlantic (triangles) and Indo-Pacific (squares) derived from the basin-wide hydrographic sections compiled by Bryden and Imawaki (2001), who give ±0.3 PW as the uncertainty in careful estimates. Their North Atlantic section between Ireland and Greenland is not included, because it excludes the Labrador Sea. The estimate plotted at 45°S is actually from a section going south–west from Cape of Good Hope before following 45°S to South America. Some of the similarly estimated ocean freshwater transports from Wijffels (2001) are shown in Fig. 10b for the Atlantic (triangles), the Indo-Pacific (squares) and the globe (diamonds), but uncertainties are only given for the latter. Not included are her freshwater transports derived using more than just ocean hydrography.

Heat conservation says that the 2.3 W/m$^2$ global heat flux imbalance (Sect. 4.1; Table 3) must be due to a combination of flux bias (including the neglect of ice–ocean heat flux) and oceanic heat storage, but the global distribution of the bias/storage is unknown. The simplest

assumption (I) is that it is uniformly distributed. The second (II) is that it is all in the Southern ocean, where observations are most scarce. More consistent with the estimated oceanic heat transports is the assumption (III) that there is no bias/storage in the Atlantic basin, and a uniform 3.0 W/m$^2$ distribution elsewhere. The resulting implied northward heat transports are shown in Fig. 10a. Applying the same procedure to each of the 23 individual years (1984–2006) produces considerable interannual variability, and at each latitude the range in global heat transport is given by the shaded envelope about the global implied heat transport curve (black). All the above assumptions ensure zero heat transport at both the North Pole and the ocean's southern limit; neglecting the approximate 0.02 PW of heat required to melt Antarctic ice entering the ocean.

In the Atlantic, assumptions II and III, both give the same curve (red). It passes within ±0.1 PW of all the oceanic estimates. This agreement is better than expected given the uncertainty in the estimates and the interannual variability. Assumption I effectively removes 2.3 W/m$^2$ more heat from the Atlantic, so that at all latitudes the implied northward heat transport would increase to supply this loss. The increases are about 0.20, 0.15, 0.12 and 0.10 PW across 30°S, 11°S, 15°N and 26°N, respectively. They are indicative of how much implied heat transport depends on bias/storage assumptions. Note that with assumption I, the increased implied transports become systematically larger than the Atlantic estimates, and beyond their stated uncertainty at 30°S.

In the Pacific, there is no known plausible bias/storage assumption that would lead to implied southward heat transport, as suggested by the oceanic estimate across 48°N (Fig. 10a). Accounting for ocean cooling via ice–ocean fluxes in the Bering and Okhotsk seas would make the disagreement worse. Farther south, assumption III (blue curve) gives excellent agreement at 9°N and is only 0.12 PW lower than the oceanic estimate (square) at 26°N. At these latitudes uniform bias/storage (assumption I) reduces the transports by <0.04 PW. With no bias and storage in the Indo-Pacific (e.g. assumption II) there is a larger effect, with the respective implied transports at these latitudes becoming systematically lower than the oceanic estimates by about 0.2 PW at both latitudes, but still within the uncertainty.

The net ocean surface heat flux $Q$ can be inferred as the small residual between the much larger terms of the top of atmosphere radiation and atmospheric heat budgets. In particular, Trenberth and Caron (2001) and Fasullo and Trenberth (2008) compute these budgets from various radiation products and reanalyses, but spatial integrals of $Q$ reveal notable differences from the CORE.v2 results (Fig. 10a). According to these three products, the respective heating between 11°S and 15°N is 3.3, 2.9 and 2.4 PW, with 36, 41 and 20% of this heat transported to the south, respectively. There is better agreement in the inferred transport to the north across 15°N (2.1, 1.7 and 1.9 PW, respectively), which is just the amount lost back to the atmosphere at higher latitudes. All three calculations show a net heating between about 45° and 55°S of about 0.2, 0.1 and 0.3 PW, respectively.

In order to compute the implied freshwater transport from CORE.v2 fluxes, river runoff is distributed over the coastal ocean and concentrated at river mouths according to observed stream flow. With such a small net freshwater flux (−0.1 mg/m$^2$ per second; Table 3) there is little sensitivity to how this bias/storage is distributed, so only a uniform distribution is assumed. There is then excellent agreement in Fig. 10b between the oceanic estimate at 45°N and the total air–sea freshwater flux plus runoff at higher latitudes, both globally and in the partition between Atlantic and Pacific. There is similar agreement at 24°N. However, in between at 35°N the oceanic estimates in both basins, and hence globally become suddenly much more southward than implied. In order to agree the freshwater fluxes would need to increase (more net precipitation) between 35°N and 45°N, and decrease (more net evaporation) between 35°N and 24°N in both basins. There is no obvious explanation for such a flux bias pattern. Possibly the disagreement at 35°N is associated with the oceanic transport estimates across the deep western boundary current portions of both basins.

At 10°N the agreement is again excellent in the Indo-Pacific, but not so good in the Atlantic, such that the implied global and Atlantic transports are 0.20 Sv more northward (Fig. 10b). In the Atlantic between 10°N and 11°S are the ITCZs and large freshwater discharge from rivers like the Amazon (0.19 Sv) and Congo (0.04 Sv). Accordingly, both the implied and oceanic transport estimates give a net freshwater input between these latitudes that is about 0.30 Sv from both these independent estimates, because at 11°S there is also about a 0.20 Sv transport difference.

In the South Atlantic Fig. 10b shows that this difference grows to 0.35 Sv at 19°S, then shrinks to 0.16 Sv at 30°S. Thus, the meridional divergences between 30°S and 11°S, which directly reflect the freshwater flux and runoff between these latitudes are quite similar (0.43 Sv vs. 0.38 Sv). At 32°S the ocean estimate for the Indo-Pacific is also less northward than the implied. Therefore, both basins contribute to a larger implied global transport across these latitudes. Possible contributors to this global discrepancy are too little evaporation from the ocean south of 19°S, uncertainty in the direct estimates, freshwater storage in the Southern Ocean and the mismatch in years. Less likely is excess precipitation, because GCGCS is on the

low side of the climatologies in Fig. 5, and including the amount that falls onto Antarctic sea-ice would make matters worse.

## 5 Comparisons of climatological fluxes

The most meaningful comparisons of fluxes from different sources are of the global distributions (Sect. 4.2), and would take into account differences in input data, in methodology (e.g. bulk formulae) and in time period. Such a comparison has been initiated (M. Bourassa, personal communication, 2007) and will include the fluxes from the present study. Nevertheless, regional flux comparisons can also be informative. For example, comparison of the unaltered NOC1.1 heat flux with surface buoy data and ocean transport estimates revealed that closure of the global ocean heat budget required regional adjustments, rather than just a uniform 30 W/m$^2$ reduction (Josey et al. 1999). Therefore, in order to give some impression of how CORE.v2 fluxes differ from alternatives, a limited comparison follows; first of zonally averaged wind stress components (Fig. 11), then of regional averages of heat fluxes (Fig. 12) and finally of freshwater fluxes (Fig. 13). A caveat of these comparisons is that there is neither a standard methodology (e.g. bulk formulae), nor time period. At high latitudes, the treatment of sea-ice is a further complication, with not all sources using ice concentration to give just the air–sea fluxes of (1); hence the latitude limits of Fig. 11. Zonal averages of stress over the Indian Ocean sector are not shown in Fig. 11, because in the Southern Hemisphere westerlies the difference pattern is very similar to those shown for the south Atlantic and Pacific, and farther north in the Indian basin all the sources are in good agreement in both components.

The climatological CORE air–sea wind stress of Fig. 6 uses winds that have been modified to agree with QSCAT winds, but they will differ from QSCAT stresses due to time period and to bulk formula differences from the "Appendix". Any such effects in CORE versus NCEP differences combine with the effects of increasing the wind speed by the factor $R_S$ (Fig. 2a). For example, these wind increases are more than compensated by the larger NCEP drag coefficient (Smith et al. 2001), so that in the westerly wind belts, especially over the Southern Hemisphere, zonally averaged stresses (Fig. 11) from NCEP (cyan trace) have systematically larger eastward and poleward components than those from CORE (black trace). In the tropical Pacific, the differences between these traces are greatly effected by the wind direction shift (Fig. 2b). Most notable is that the nearly uniform convergence in the meridional NCEP stress between 10°S and 10°N, becomes concentrated north of about 3°N, and hence more consistent with the ITCZ precipitation of Fig. 7a. Despite the higher drag coefficient and more westward direction, the NCEP westward stress in this region is much smaller than CORE, because of the large wind speed correction (Fig. 2a).

In general, the zonal average stresses from CORE and ERA-15 (red traces) track each other more closely than they do NCEP. The agreement is particularly close in both components throughout the tropics. The most notable exceptions are the zonal stresses in the westerly wind belts, but ERA15 stresses are stronger in some basins (South Atlantic, South Indian, North Pacific) and weaker in others (North Atlantic, South Pacific), so it is not a simple bulk formula issue. ERA40 stresses (not shown) are similar to ERA15, expect in the Pacific sector where their Southern Ocean westerlies are even stronger than NCEP and their easterlies between 10°S and 10°N are weaker than both ERA15 and CORE.

Shipboard wind observations are the bases of both the NOC1.1 (blue traces) and the HR (Hellerman and Rosenstein 1983) wind stress climatologies shown in Fig. 11. Their differences have been discussed by (Josey et al. 2002), who find the choice of drag coefficient in (3a) to be a major contributor. All across the southern Hemisphere westerlies these two climatologies differ significantly with each other, with both reanalyses and with CORE, likely because of the poor ship sampling (Josey et al. 2002). Sampling may also be an issue around 50°N, where the higher global HR zonal stress farther north comes from the Pacific, while to the south it and the low NOC zonal stress comes from the Atlantic. The two ship-based climatologies also differ greatly from each other and from the other products in meridional stress in the South Atlantic, South Pacific and North Pacific. In the tropics, the weak global westward stress of NOC1.1 arises almost entirely from the Pacific sector, where HR, ERA15 and CORE are in close agreement.

Roske (2006) compares his OMIP heat and freshwater fluxes to a number of available alternatives, including the original ERA15, both versions of NCEP reanalyses over the same 15 years, the adjusted NOC1.1a climatology, 15 years of output from the ECHAM atmospheric GCM (Roeckner 1996) and the second version of HOAPS. The freshwater flux comparison also includes CMAP and GPCP precipitation. His 20 regions mostly correspond to the global partitioning of MacDonald and Wunsch (1998), except their Atlantic/Arctic region is divided into two by a line from the southern tip of Greenland to Ireland. This and other non-land region boundaries coincide with hydographic sections, across which ocean heat and freshwater transports can be estimated. Differences (divergences) in these transports give independent measures of the average net heat flux, $Q$ in (1c), over these regions, and those inferred by MacDonald and Wunsch (1998) are included in

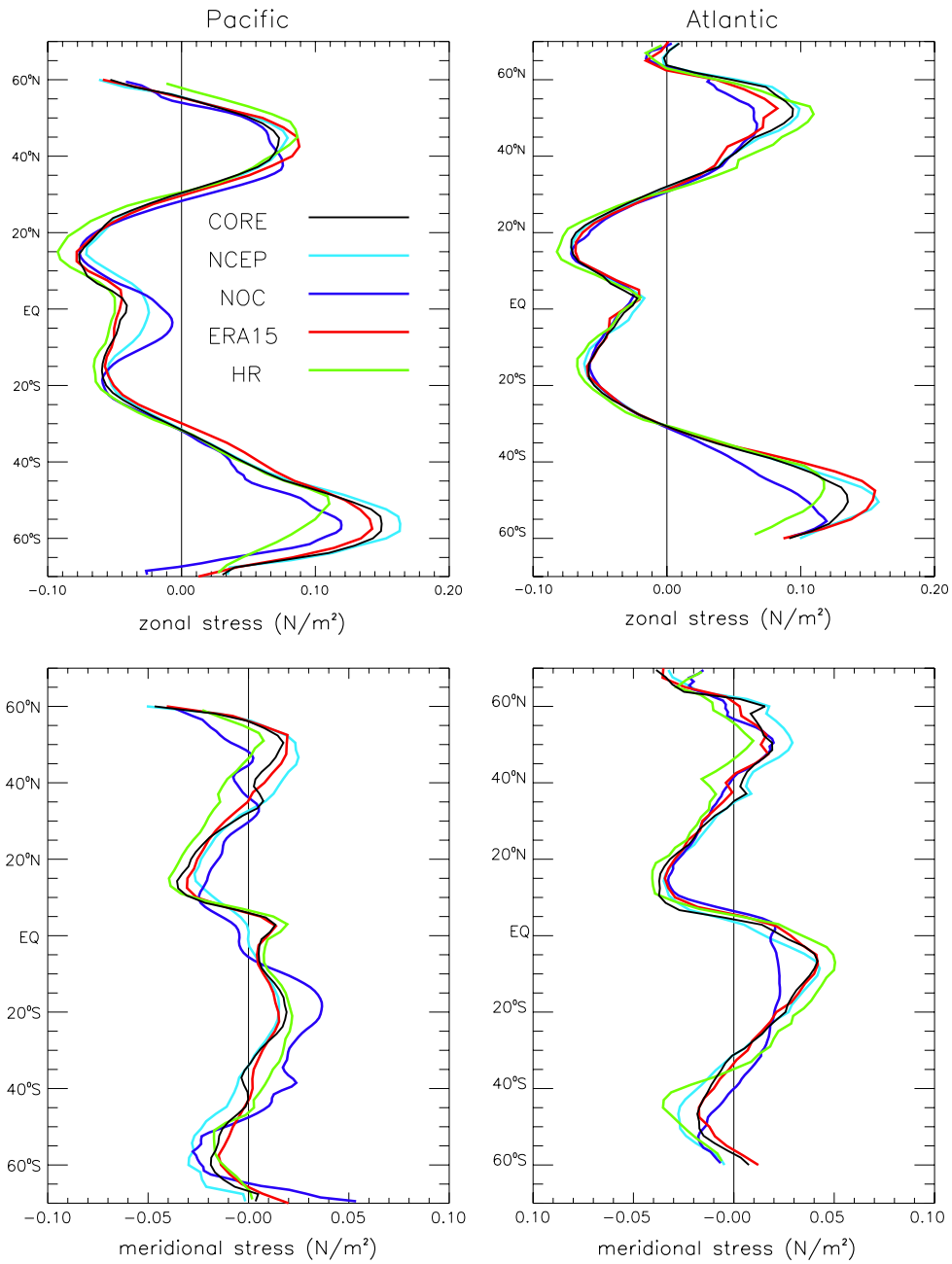


**Fig. 11** Zonal averages of climatological CORE.v2 wind stress components (*black traces*) over the Atlantic (295°E–20°E) and Pacific (155°E–255°E) ocean basins. The other data sources (NCEP, NOC1.1, ERA-15 and HR) are described in the text

the comparison. For some purposes, it is convenient to combine Roske's South Atlantic regions 8, 9 and 10, as in Fig. 12, and also to split his tropical Indo-Pacific region 13 into Indian (13I) and Pacific (13P) sectors.

Table 4 shows the results of Sect. 4.2 as averages over all these regions and sub-regions of the climatological CORE.v2 heat and freshwater fluxes plus runoff and their components. The regional averaging obscures smaller scale features such as the heat losses associated with Western Boundary Currents (Fig. 8) and the ITCZ precipitation (Fig. 7b), so the global maps of Figs. 7, 8 and 9 are required for more detailed comparisons.

For the 18 regions of Fig. 12, the various net heat fluxes and their components, as compiled by Roske (2006), are shown as differences from Table 4 CORE values, such that a zero value along the horizontal axis indicates perfect agreement in the mean. For each flux, the vertical line spans the range from the maximum to the minimum difference. In addition, OMIP (red triangles) and NOC1.1a (blue crosses) differences are plotted individually. A disturbing feature of Fig. 12 is the $\pm 40$ W/m$^2$ range required for the vertical axes. This range is too large to be indicative of the uncertainty in individual heat flux components from all sources, with the implication that some estimates should

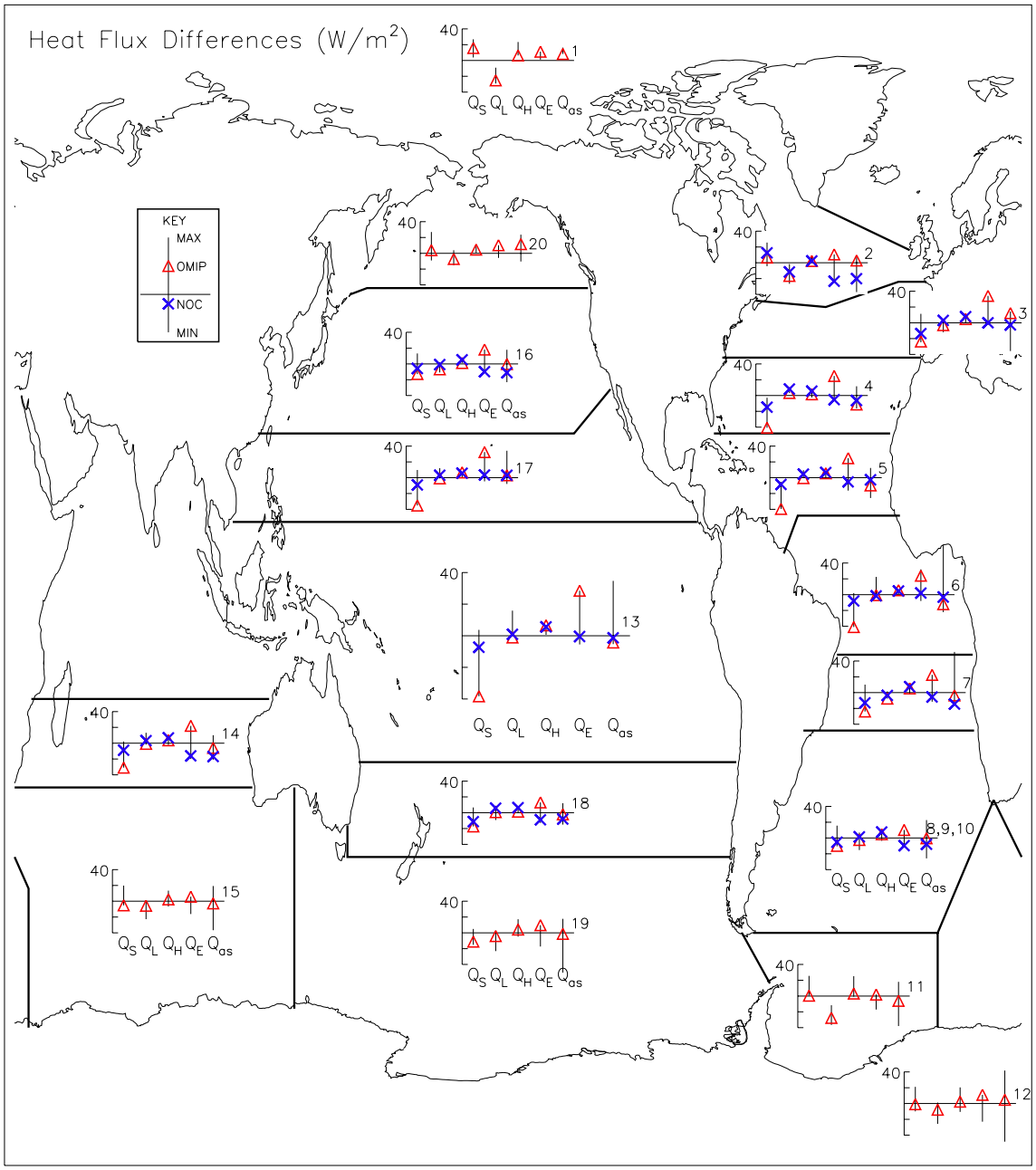


**Fig. 12** Regional comparison of climatological net heat flux and its components. The differences are from the CORE.v2 air–sea fluxes of Table 4 in W/m$^2$. The OMIP and NOC1.1a values are shown as *red triangles* and *blue crosses*, respectively, and the *vertical lines* indicate the range in the data sets compiled by Roske (2006). The region numbers are given to the *right of each axis*

be discounted as being outside an acceptable range, but this range has yet to be agreed upon. In the meantime virtually every flux estimate can find another that is within an acceptable level of agreement. Also, it can be argued that detailed comparison issues, such as using common years and methodology, need not be considered until this range has been reduced to about 10 W/m$^2$.

A major contributor to the large range in the net heat flux, $Q_{as}$, is the inclusion of the fluxes given by divergence of the MacDonald and Wunsch (1998) ocean transport estimates. These fluxes are at the minimum of the range in 6 regions (3, 5, 8, 9, 16, 18), at the maximum in four other regions (7, 10, 12, 14), and within 3 W/m$^2$ of the minimum in region 15 and of the maximum in region 4. Therefore, they can be considered as outliers, though not necessarily incorrect, in 12 of Roske's 20 regions. Region 10 is the worst case with the transport divergence giving 100 W/m$^2$ more ocean heating than any other data set, including

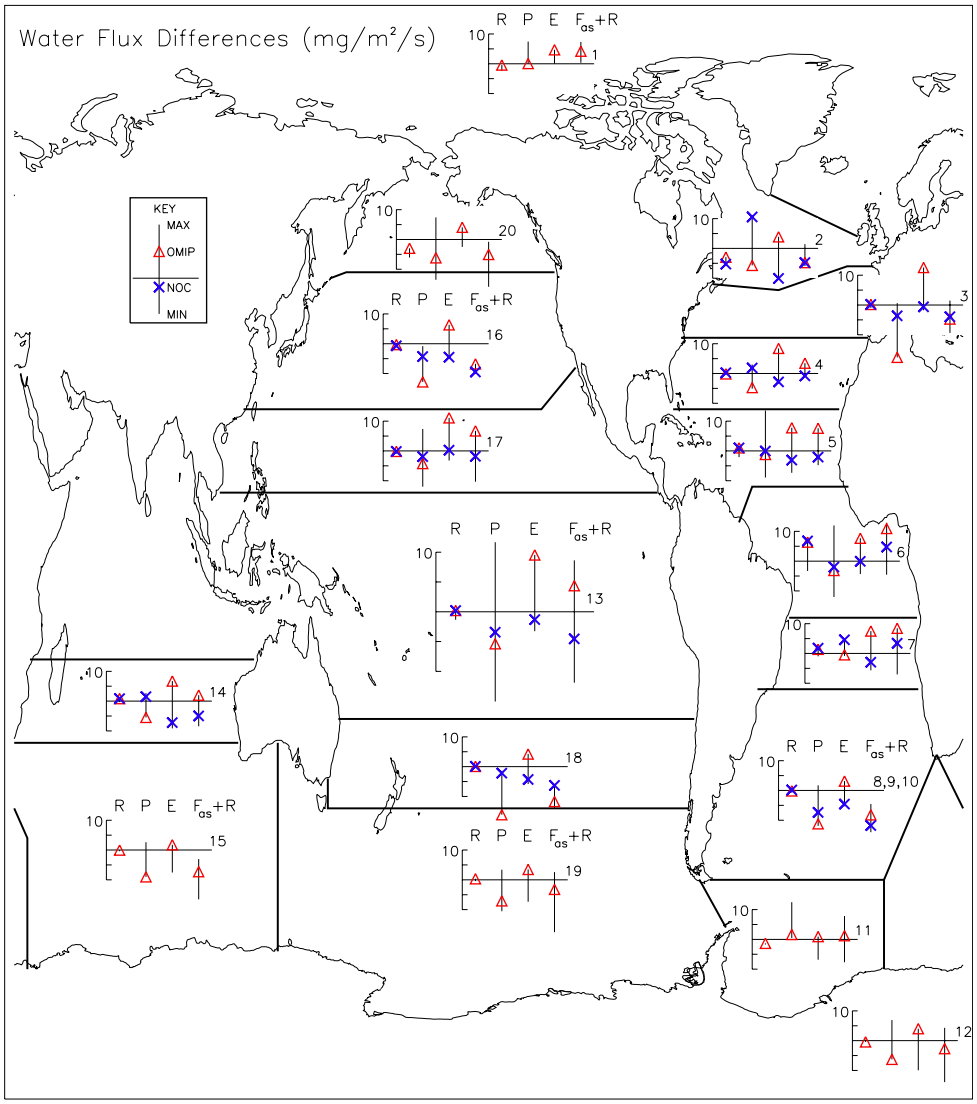


**Fig. 13** As Fig. 12, but for the climatological net freshwater flux and its components, plus river runoff. The units are mg/m$^2$ per second

CORE. This problem is obscured in Fig. 12 by combining this region with regions (8 and 9) where the transport divergence gives the minimum heating.

There is significant ice cover (Fig. 1) in seven regions (1, 2, 11, 12, 15, 19 and 20), where CORE fluxes depend greatly on the definition (1) that includes only the ice-free area. Comparisons in these regions are complicated by different treatments of ice cover. In particular, it is not accounted for in NOC1.1a, which is therefore excluded from the comparisons in these regions. In general, OMIP differences in the sea ice regions are smaller than elsewhere, presumably because the differences in air–sea fluxes are multiplied by $f_0$ and tend to zero as the ice concentration goes to 1. In regions 12, 15, 19 and 20 each OMIP and CORE heat flux, net and component, are all within $\pm 10$ W/m$^2$, and a more refined comparison should include standard ice treatments and common years. In the other icy areas (1, 2 and 11), only the $Q_L$ difference is outside this range at between $-20$ and $-30$ W/m$^2$, and the respective $f_o Q_L$ values of $-26$, $-39$ and $-23$ W/m$^2$ are the three least negative values in Table 4. The global maps of Figs. 1 and 9b show that these low values are indeed from regions with considerable sea-ice cover.

In all ice free regions of Fig. 12 a general pattern emerges. The relatively small OMIP differences ($\pm 15$ W/m$^2$) in the net heat fluxes, $Q = Q_{as}$ (1c), are a fortunate consequence of very large positive differences in $Q_E$ compensating for similarly large negative differences in $Q_S$. In every ice free region, OMIP is at or very near the minimum solar radiation, with NOC1.1a differing less from CORE, and in all but two (7 and 18) $Q_S$ from NOC1.1a is in better agreement with CORE than with OMIP. In the tropics (regions 6 and 13) OMIP solar radiation is about 40 W/m$^2$ less than CORE, even after the 5% reductions made to $Q_I$ (Sect. 3.2), and hence 40 W/m$^2$ less than has

**Table 4** Regional climatological CORE.v2 air–sea heat flux (W/m$^2$) and freshwater flux plus runoff (mg/m$^2$ per second), and their components over 23 years (1984–2006)

| | $f_oQ_{as}$ | $f_oQ_S$ | $f_oQ_L$ | $f_oQ_H$ | $f_oQ_E$ | $f_oF_{as} + R$ | $f_oP$ | $f_oE$ |
|---|---|---|---|---|---|---|---|---|
| 1 | −33 | 37 | −26 | −18 | −26 | 8 | 10 | −11 |
| 2 | −26 | 84 | −39 | −23 | −47 | 16 | 28 | −19 |
| 3 | −41 | 149 | −59 | −23 | −108 | 2 | 42 | −43 |
| 4 | −17 | 193 | −70 | −15 | −125 | −21 | 28 | −50 |
| 5 | 6 | 216 | −62 | −13 | −135 | −21 | 26 | −54 |
| 6 | 35 | 216 | −51 | −10 | −120 | 12 | 38 | −48 |
| 7 | 20 | 210 | −55 | −12 | −123 | −38 | 8 | −49 |
| 8 | 26 | 201 | −59 | −11 | −104 | −29 | 12 | −42 |
| 9 | 5 | 142 | −58 | −11 | −69 | 12 | 37 | −27 |
| 10 | 18 | 152 | −52 | −12 | −70 | −8 | 19 | −28 |
| 8, 9, 10 | 8 | 148 | −57 | −11 | −71 | 6 | 32 | −29 |
| 11 | 1 | 49 | −23 | −12 | −13 | 7 | 10 | −5 |
| 12 | −3 | 95 | −42 | −13 | −42 | 8 | 24 | −17 |
| 13 | 19 | 214 | −55 | −12 | −129 | 0 | 48 | −51 |
| 13P | 24 | 213 | −54 | −12 | −124 | 1 | 49 | −50 |
| 13I | 8 | 217 | −58 | −12 | −139 | −3 | 47 | −56 |
| 14 | −18 | 203 | −66 | −18 | −137 | −33 | 20 | −55 |
| 15 | 2 | 120 | −49 | −13 | −56 | 7 | 28 | −22 |
| 16 | −16 | 154 | −54 | −18 | −97 | 6 | 42 | −39 |
| 17 | 1 | 209 | −57 | −13 | −138 | −14 | 40 | −55 |
| 18 | −5 | 163 | −64 | −13 | −91 | 3 | 39 | −36 |
| 19 | −2 | 96 | −46 | −13 | −39 | 10 | 25 | −16 |
| 20 | −12 | 97 | −46 | −22 | −40 | 22 | 30 | −16 |

The regions are shown in Figs. 12 and 13

been measured at the TAO/PIRATA buoys. This result supports the exclusion of NWP radiation products from the present study and illustrates the significance of the consequences. A final feature of the overall pattern is that differences in longwave radiation and sensible heat flux are typically much smaller (±10 W/m$^2$) and will warrant a detailed comparison only after solar and latent heat flux differences are resolved.

The freshwater flux comparison of Fig. 13 is complicated by the continental runoff (1b), which can be calculated from Table 4 by subtracting the sum of the $f_0P$ and $f_0E$ columns from the $f_0F_{as} + R$ column. As described in LY04, this runoff is based on observed estimates of precipitation and evaporation over the continents and is distributed to the ocean according to continental topography and the observed discharge from guaged rivers. The OMIP runoff is based on ERA15 precipitation and evaporation over the continents, with ad hoc daily balancing, and is distributed according to continental topography. Roske (2006) notes extreme differences between the resulting river discharge and observations. Notable examples are the excessive flows of both the Congo and Niger rivers, which are responsible for the large positive OMIP runoff difference (5 mg/m$^2$ per second) in region 6. Negative differences of nearly this magnitude are seen in regions 2 and 20, into which many rivers empty. These consequences of using ERA15 precipitation over land support the exclusion of any NWP precipitation in the present study.

An expected feature of Fig. 13 is that the OMIP latent heat flux differences are reflected in the evaporation differences, which are typically large and at or near the maximum in all ice free and ice covered regions. In every ice free region NOC1.1a evaporation, and hence latent heat flux (Fig. 12), is in closer agreement with CORE than with OMIP. A key finding in the case of the freshwater budget is that the less negative OMIP evaporation is not everywhere compensated by less precipitation, so there are regions (1, 5, 6, 7, 17) where the OMIP net freshwater flux and evaporation differences are comparably large and positive. In other regions (2, 8, 9, 10, 12, 15, 16, 18, 19 and 20) OMIP precipitation is at or near the minimum, more than 5 mg/m$^2$ per second less than CORE and little compensated by evaporation plus runoff, such that the net freshwater flux differences are about −5 mg/m$^2$ per second, or worse.

## 6 Basin scale trends and variability

A prime motivation for producing the CORE.v2 air–sea flux data is its interannual variability. As a first demonstration of this feature, it is now exploited to show how the heat and freshwater fluxes vary from year to year on basin to global scales. This variability from 1950 to 2006 is shown in Fig. 14 as annual means of global and basin average heat and freshwater fluxes. Before proceeding, it is important to recall some possible sources of spurious or suppressed variability. The annual radiation is constant prior to 1984, as are precipitation and sea-ice before 1979. The nature of the data assimilated by the NCEP reanalysis and utilized in producing the SST is steadily evolving, with a fundamental change in the 1970s with the advent of the satellite era. The applied adjustments may not be valid over the whole of this 57-year period.

The most prominent basin scale, low-frequency variability is seen in the heat flux (Fig. 14a). It implies cycles of ocean heat storage and release that are more likely balanced by the net radiative heat flux through the top of the atmosphere, than atmospheric heat storage. It also illustrates that global heat budgets (e.g. Table 3) depend on the time period. The 57-year average (±1 SD) is 3.3 ± 2.8 W/m$^2$. The largest decadal average (1977–1986)

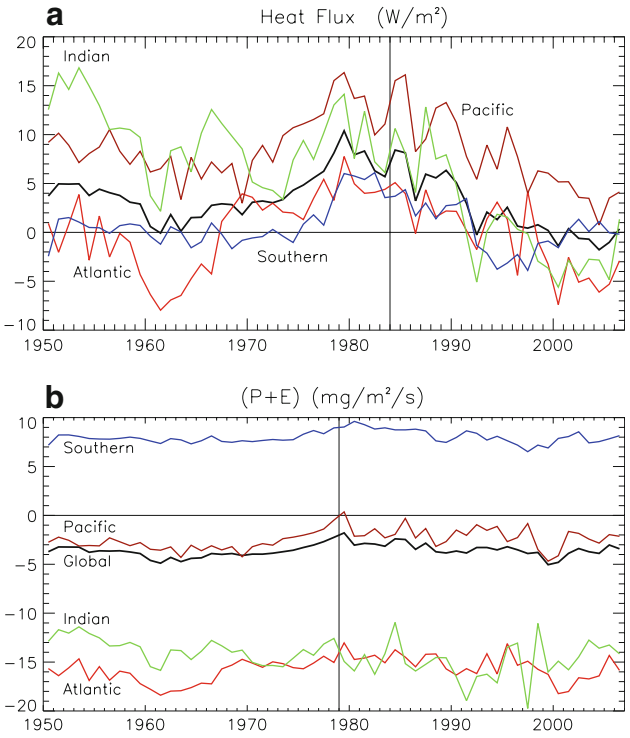


**Fig. 14** Time series over 57 years (1950–2006) of annual mean CORE.v2 fluxes averaged over the global ocean and the Atlantic, Pacific, Indian and Southern, but not the Arctic basins: a air–sea heat flux in W/m$^2$, b air–sea freshwater flux, excluding runoff, in g/m$^2$ per second

is 7.3 ± 2 W/m$^2$ and the smallest (1997–2006) is −0.3 ± 1.3 W/m$^2$. All basins contribute to the variability. The reduced heating of the 1960s is mainly due to Atlantic cooling and less Pacific heating. After peaking around 1980, the heat flux into all ocean basins tends to decrease through 2006, especially in the Indian.

There are no extra-terrestrial sources of freshwater, and little atmospheric storage capacity. Thus, interannual variations in global net freshwater flux are constrained and the global balance (Fig. 14b) is not very dependent on time period. This variability is similar in the Pacific and Southern Oceans, and only somewhat stronger in the Indian and Atlantic basins. As expected, it does increase, but not by much, after 1979 when the precipitation becomes variable.

The Atlantic basin is a net source of water for the atmosphere (Baumgartner and Reichel 1975), and this balance and its variability after 1979 are quantified in Fig. 14b by the mean (±1 SD) of −15.3 ± 1.3 mg/m$^2$ per second. Similarly, the Indian ocean loses freshwater over these 28 years, but at a mean rate of −15.0 ± 2.0 mg/m$^2$ per second. A near global balance is achieved by continental runoff and by net freshwater input into the Southern ocean (8.1 ± 0.8 mg/m$^2$ per second).

## 7 Discussion and conclusion

A very large number and variety of observed data feed, either directly or indirectly, into the CORE.v2 air–sea fluxes computed for this study. Nevertheless, these fluxes do not, strictly speaking, constitute an observational flux data set, because the NCEP reanalysis products depend on the NWP model and data assimilation system, the ISCCP-FD surface radiation is computed using a radiative transfer model (RTM), and satellite retrievals of SST, vector wind, sea-ice and precipitation are indirect. Another issue with the precipitation is that the behavior of a particular ocean model guided the regional choices of precipitation data sets, but affected neither the variability, nor the factor 1.14 increase of the satellite products. Although the SST reconstructions before the advent of the satellite era in about 1979 utilize available observations, values are filled over large under sampled, or even data void regions.

The resulting CORE.v2 fluxes depend on a number of choices regarding the base data (e.g. NCEP, ISCCP-FD), the reference data (e.g. QSCAT, TAO buoys), what variables to adjust (e.g. vector wind, solar radiation), the space–time dependencies of adjustments, and comparisons of specific rather than relative humidity. The particular choices made represent one particular judgment, but there are equally justifiable alternatives that would give somewhat different results. At least the choice of reanalysis data set should not be overly critical, because of the adjustments to the reference data and the exclusion of NWP products that directly involve clouds; namely, radiation and precipitation. The reasoning is that observed clouds are not assimilated, so NWP cloud fields are unconstrained and potentially seriously in error. This position is supported by the comparisons of precipitation (Fig. 5), solar radiation (Table 2; Beranger et al. 1999) and OMIP fluxes (Figs. 12, 13). It may also explain the failure of attempts to find large scale, stable difference patterns between the earlier ISCCP products used in Large et al. (1997) and NCEP radiation. Such patterns could form the basis for NCEP adjustments that would generate interannual variability in radiation prior to 1983. In order to maintain consistency, this methodology would need to be successful for both $Q_I$ and $Q_A$, but only the latter showed any promise. At that time, the methodology was not attempted for precipitation, because of the limited and inconsistent reference data. Now the ISCCP-FD radiation and the merged GCGCS precipitation could give more success, if not for NCEP then perhaps for other reanalyses.

A great advantage of the CORE methodology is that specific choices can be easily altered in response to experience (Griffies et al. 2008) and to new observational data. In practice, this ability has produced differences from CORE.v1, in addition to the 6-year extension through

2006. The major departures are the wind rotation (Fig. 2b) and the adjustment to specific, rather than relative humidity (Fig. 3). The minor modifications are the speed factor (Fig. 2a) from 5 years of QSCAT instead of 2, the latitudinally dependent albedo (Fig. 4), and the global gain (1.1427) and offset (0.7 mg/m$^2$ per second) applied to precipitation has become just a gain (1.14) applied to satellite products only. Since CORE.v2 choices were finalized reference data sets have continued to expand and evolve. As an example of expansion, global precipitation and evaporation from 1987 to 2007 are derived from satellite Special Sensor Microwave Imager measurements by Wentz et al. (2007). Although air–sea fluxes are not given directly, the mean ocean evaporation can be inferred to be about −41.4 mg/m$^2$ per second, or about 3 mg/m$^2$ per second more negative than CORE.v2. The NOC climatology is now at version 2.5, but before any updates to the $\delta q$ adjustment, for example, further consistency checks with independent data would be required. Version 3 of HOAPS may have improved the precipitation, but would not be independent of any other products that influenced the changes. There are also multiple versions of OAflux, but they are all optimal blends of various data and therefore more of an alternative to CORE fluxes, rather than reference data.

The accuracy of the computed flux components depends implicitly on the fidelity of the reference data, such as QSCAT, NOC humidity and TAO radiation, on which the Sect. 3 adjustments were based and verified. However, the complexity of the entire data flow, the nature of the adjustments and the sparse distribution of in situ flux measurements in both time and space all conspire to make a more comprehensive error analysis than contained in Taylor (2000) and the comparisons of Sect. 5, beyond the scope of the present work. Although ocean inventories indicate that the calculated global mean heat and freshwater fluxes are accurate to within a few W/m$^2$ and about a mg/m$^2$ per second, respectively, there is almost certainly considerable cancellation of large regional errors, with $Q_I$ of Table 2 a prime example.

Despite the uncertainties, the meridional distribution of basin scale fluxes is in very close agreement with independent ocean transport estimates (Fig. 10). For example, the good match of Atlantic heat transport at 26°N is not forced and is perhaps better than expected for all three of the bias/storage assumptions. The overall agreement is closer than CORE.v1 results (LY04), because of differences in time period, humidity correction, albedo and storage/bias assumption. The atmospheric residual heat transport calculations of Trenberth and Caron (2001) and Fasullo and Trenberth (2008) would be in better agreement south of 15°N without the 5% reduction of ISCCP-FD solar radiation, provided most of the extra tropical heating was lost from the Southern Ocean (Sect. 4.3, assumption II). However, there is no other evidence to support such a heat loss, the buoy comparison (Table 2) is evidence against additional solar heating in the tropics and the agreement with Atlantic oceanic transport estimates at 15°N and 11°S (Fig. 10a) argues against any additional heating of the Atlantic between these latitudes. There are large discrepancies in freshwater transport across 35°N in both the Atlantic and Pacific, and hence globally (Fig. 10b), but the very good agreement both to the north and south suggest revisiting the observationally based estimates, especially the transports by the western boundary currents.

A detailed comparison of the spatial flux maps with the many available alternatives is beyond the scope of the present study, and would be largely redundant with those of (Taylor 2000) and (Beranger et al. 1999), with similar findings likely. Nonetheless, the maps of Sect. 4.1 do facilitate comparison with the alternatives contained in these two works, and with more recent products such as OAflux (Yu and Weller 2007). There must be regions where at least early versions of OAflux have a very different heat flux, because of the global imbalance. Similarly, there are large differences from the ship based NOC1.1 heat flux, because of its $\approx$30 W/m$^2$ global imbalance (Sect. 4). The area of much greater NOC1.1 heating includes the TOGA COARE region of the western tropical Pacific, where it gives 60 W/m$^2$ heating compared to less than 25 W/m$^2$ in Fig. 8. Observational and ocean budget estimates (Gent 1991) place the net heat flux at between 10 and 20 W/m$^2$. In region 17 of Fig. 12 NOC1.1 gives an average heat flux of 46 W/m$^2$, compared to 2 W/m$^2$ from ocean transports (Josey et al. 1999) and from CORE.v2 (Table 4). Therefore, the large change of the NOC1.1a inversion appear to be a great improvement in the air–sea heat flux in this region of the tropical Pacific (Fig. 12).

The present suite of air–sea fluxes is consistent in that the same wind is used to compute the stress (3a), sensible heat flux (3d) and evaporation(3b), and the latter is physically linked to the latent heat through (3c). This physics can be lost when the fluxes themselves are adjusted, as with the flux increments of Stammer et al. (2004), or ocean transport based inversions. Also, cloud error in the RTM calculations will often tend to be of opposite sign in the two radiation components, with a large degree of cancellation possible. Another attractive feature is that the adjusted NCEP atmospheric state, ISCCP radiation, merged precipitation and if necessary, sea-ice concentration data sets were assembled to force ocean and coupled ocean-ice (e.g. CORE) models. Any resulting differences in modeled versus computed fluxes would primarily be a quantitative measure of the significance of SST departures from the Hadley-OI data. Despite the common forcing the first

CORE results show significant differences in ocean model behavior (Griffies et al. 2008).

There is little justification for applying the same corrections, every year. The advent of the satellite era in the late 1970s may have introduced spurious time dependencies. The corrections of Sect. 3 affect the heat flux by more than the magnitude of the decadal variations of Fig. 14. Therefore, these signals have considerable uncertainty and can at best be considered a measure of relative change. The 1984–2006 period used in the balancing of Sect. 4.1 includes years of both relatively large and small global heating. Therefore, the 2 W/m$^2$ imbalance is similar to the 3 W/m$^2$ global imbalance over the full 57-year period. However, the danger in determining balances over short periods, such as 1977–1986 for example, is clearly shown in Fig. 14. The difference compared to a period such as 1997–2006 is nearly 8 W/m$^2$.

The utility of global air–sea flux data sets is limited by the large range in mean values from available products. For example, the range in heat flux estimates across the tropical Pacific means they are not very useful in assessing the behavior of coupled climate models in this important region of air–sea interaction (Wittenburg et al. 2006). Even zonal averages of mean stress components (Fig. 11) span an unacceptably large range especially in the Southern Ocean and the tropical Pacific. In the regional comparisons of heat (Fig. 12) and freshwater (Fig. 13) fluxes, the range often exceeds 40 W/m$^2$ and 10 mg/m$^2$ per second. It should be possible to reach a consensus where acceptable fluxes would need to fall into a much smaller range. It would first be necessary to adopt a consistent treatment of ice cover and to reconcile the results of ocean inversions (MacDonald and Wunsch 1998) and ocean transport estimates (Fig. 10). At the point the accepted ranges approach 10 W/m$^2$ and 5 mg/m$^2$ per second, factors that will then need to be considered more carefully include sensible and longwave heat flux differences, the cooling of rain, snow and icebergs, differences in methodology, time period (Fig. 14), and ice–ocean fluxes.

**Acknowledgments** This work was supported by NOAA grant no. NA06GP0428 and by the National Science Foundation through its sponsorship of the National Center for Atmospheric Research. It could not have proceeded without the heroic efforts of all the individuals responsible for producing the individual data sets we have utilized. In particular we thank Y. Zhang and W. Rossow for early access to the ISCCP-FD products.

## Appendix: Bulk transfer coefficients

The bulk transfer coefficients as defined by Eq. 3 depend on height above the surface, atmospheric stability and surface roughness lengths for momentum, $z_o$, evaporation, $z_q$, and heat, $z_\theta$. In an ideal world of plentiful, reliable flux measurements, coefficient estimates would be binned according to height and stability, so that further roughness dependencies, for example on the wind speed and sea state (Bourassa et al. 1999), could be determined for each bin. Unfortunately, direct flux estimates are too difficult, expensive and rare. Therefore, most coefficient determinations are shifted to a standard reference height of $Z_r = 10$ m and neutral stability, where the three coefficients become;

$$C_{\mathrm{DN}} = \frac{\kappa^2}{[\ln(\frac{Z_r}{z_o})]^2}; \quad C_{\mathrm{HN}} = \frac{\kappa\sqrt{C_{\mathrm{DN}}}}{\ln(\frac{Z_r}{z_\theta})}; \quad C_{\mathrm{EN}} = \frac{\kappa\sqrt{C_{\mathrm{DN}}}}{\ln(\frac{Z_r}{z_q})} \qquad (9)$$

and $\kappa = 0.4$ is the von Karman constant. The wind speed is usually shifted to an equivalent 10 m, neutral value, $U_{\mathrm{N}}$, before searching for roughness dependencies on wind speed. The iterative procedure used to find $U_{\mathrm{N}}$ from $\Delta\vec{U}$ and for converting the above coefficients to those in (3) is detailed both in LY04 and Large (2006).

The roughness length dependencies of these coefficients have been explored using many data sets, but rarely with combined data. This search has not been conducted in a single standard way, so the procedure, rather than the data, can be responsible for differences in results. The approach adopted here follows Vera (personal communication, 1983), who combined multiple data sets to span a range of wind speeds from less than 1 m/s (Schacher et al. 1981) to more than 25 m/s Large and Pond (1981). A multivariate analysis of $|\vec{\tau}|/\rho = u^{*2}$ on integer powers of $U_{\mathrm{N}}$, gave the coefficients of the polynomial

$$u^{*2} = a_0 + a_1 U_{\mathrm{N}} + a_2 U_{\mathrm{N}}^2 + a_3 U_{\mathrm{N}}^3 + \cdots + a_n U_{\mathrm{N}}^n. \qquad (10)$$

Consistent with the principle of zero wind speed yields no net stress, this exercise gave $a_0 = 0$; with $a_1 = 0.00270$ m/s, $a_2 = 0.000142$ and $a_3 = 0.0000764$ (m/s)$^{-1}$ the only statistically significant nonzero coefficients.

However, there have been a number of more recent investigations of the behavior of $C_{\mathrm{DN}}$ at higher winds. In particular, Donelan et al. (2004) compile wind tunnel measurements and conclude that there is saturation for $U_{\mathrm{N}}$ between 33 and 50 m/s. In this range $C_{\mathrm{DN}}$ is approximately constant between 0.0022 and 0.0025. At lower speeds, the over ocean values of Large and Pond (1981), tend to be higher than the wind tunnel results, but the few data points at $U_{\mathrm{N}} \geq 25$ m/s are consistent with a leveling off. It is possible to make a smooth transition to the wind tunnel results for $U_{\mathrm{N}}$ between 30 and 33 m/s. by retaining a negative coefficient $a_8 = -3.14807 \times 10^{-13}$ (m/s)$^{-6}$ in polynomial (10).

Division of (10) by $U_{\mathrm{N}}^2$ then yields

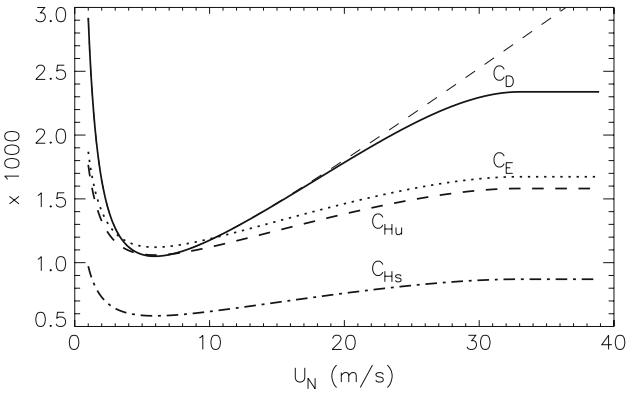


**Fig. 15** The neutral, 10 m transfer coefficients as a function of 10-m neutral wind speed, $U_N$. The drag coefficient, $C_D$, formulation follows the thick solid line, not the thin dashed extrapolation of LY04. Only $C_H$ is different in stable, $C_{Hs}$, than unstable, $C_{Hu}$ atmospheric stratification

$$C_{DN} = a_1/U_N + a_2 + a_3 U_N + a_8 U_N^6, \quad U_N < 33\,\mathrm{m/s} \tag{11a}$$

$$= 0.00234, \quad U_N \geq 33\,\mathrm{m/s} \tag{11b}$$

This formulation of $C_{DN}(U_N)$ is plotted if Fig. 15. The first derivative of (11a) is zero at $U_N$ = 33 m/s, where $C_{DN}$ equals 0.00234, compared to 0.00272 for $a_8$ = 0.0 (thin dashed line).

Recent aircraft measurements (French et al. 2007) and radiosonde profiles (Powell et al. 2003) in hurricane conditions also indicate a leveling off, or even a decrease in $C_{DN}$ at very high wind speeds. The latter show $C_{DN}$ decreasing from 0.0022 at $U_N$ = 30 m/s to about 0.0017 at 50 m/s. The former are very scattered and $C_{DN}$ is only about 0.017 for $U_N$ greater than 22 m/s, but in better agreement with Fig. 15 at lower wind speeds. Thus, these two hurricane results are inconsistent and both differ significantly from Donelan et al. (2004). Reasons for this situation may include the difficulty of measuring near surface processes in hurricanes, and different wind-wave conditions under a hurricane than under other storms or in a wind tunnel.

Over the most important wind speed range (5 m/s < $U_N$ < 15 m/s) the drag coefficient formulation of Fig. 15 tends to be larger than windtunnels (Donelan et al. 2004), about the same as the COARE 2.0 algorithm (Fairall et al. 1996) and smaller than COARE 3.0 (Fairall et al. 2003). The unbounded rise at very low winds is more rapid than given by Smith (1988).

Historically, formulations of heat and evaporation coefficients have more closely followed (10), which is rarely used to formulate the drag coefficient. Specifically, measured heat and evaporation fluxes have been regressed on $U_N$ times a 10 m, neutral air–sea temperature, or humidity difference, respectively. In the case of evaporation, the offset is not significantly non-zero, so the slope gives $C_{EN}$ directly from (3b). However, in the heat flux case there is a significant positive offset, and furthermore, the slope is found to be steeper in unstable atmospheric conditions, than in stable. Thus, it is necessary to treat stable and unstable heat fluxes separately. The positive offset is consistent with an unbounded transfer coefficient (slope) as wind speed approaches zero, but the flux, as in the case of stress (10), should diminish. This behavior can also be achieved by using fluxes to compute the roughness lengths in the form used in (9):

$$\frac{\kappa}{\ln(10m/z_\theta)} = 0.0327; \quad \text{unstable} \tag{12a}$$

$$= 0.0180; \quad \text{stable} \tag{12b}$$

$$\frac{\kappa}{\ln(10m/z_q)} = 0.0346. \tag{13}$$

There is relatively little scatter in these values (Large and Pond 1982) because much of the observed variability in measured $C_{HN}$ and $C_{EN}$ is accounted for in the drag coefficient on the right hand sides of (9). Once determined, these numbers directly give the formations of $C_{HNu}$ (unstable), $C_{HNs}$ (stable) and $C_{EN}$ shown in Fig. 15.

## References

Baumgartner A, Reichel E (1975) The world water balance. Elsevier, New York, 180 pp

Beranger K, Viau K, Barnier B, Garnier E, Molines JM, Siefridt L (1999) An atlas of climatic estimates of air–sea fluxes, 19 pp plus figures

Biastoch A, Boning C, Getzlaff J, Molines J-M, Madec G (2008) Causes of interannual-decadal variability in the meridional overturning circulation of the mid-latitude North Atlantic Ocean. J Clim (in press)

Bourassa M, Vincent D, Wood W (1999) A flux parameterization including the effects of capillary waves and sea state. J Atmos 56:1123–1139

Bryden H, Imawaki S (2001) Ocean heat transport. In: Siedler G, Church J, Gould J (eds) Ocean circulation and climate. International Geophysics Series, vol 77. Academic Press, New Yoek, pp 317–336

Cayan D (1992a) Latent and sensible heat flux anomalies over the northern oceans: driving the sea surface temperature. J Phys Oceanogr 22:859–881

Cayan D (1992b) Latent and sensible heat flux anomalies over the northern oceans: the connection to monthly atmospheric circulation. J Clim 5:354–369

Chin T, Milliff R, Large W (1998) Basin-scale high-wavenumber sea surface wind fields from multiresolution analysis of scatterometer data. J Atmos Oceanic Technol 15:741–763

Comiso J (1999) Bootstrap sea ice concentrations for NIMBUS-7 SMMR and DMSP SSM/I, Digital Media, National Snow and Ice Data Center

Curry R, Mauritzen C (2005) Dilution of the northern North Atlantic Ocean in recent decades. Science 308:1772–1774

Dai A, Trenberth K (2002) Estimates of freshwater discharge from continents: latitudinal and seasonal variations. J Hydrometeorol 3:660–687

DaSilva A, Young C, Levitus S (1994) Atlas of surface marine data 1994. NOAA Atlas NESDIS 6 (6 vols). U.S. Department of Commerce, NODC, User services branch, NOAA/NESDIS/ E/OC21

Donelan M, Haus, B, Reul N, Plant W, Stiassnie M, Graber H, Brown O, Saltzman E (2004) On the limiting aerodynamic roughness of the ocean in very strong winds. Geophys Res Lett 31. doi: 10.1029/2004GL019460

Ebuchi N, Graber H, Caruso M (2002) Evaluation of wind vectors observed by QuikSCAT/seawinds using ocean buoy data. J Atmos Oceanic Technol 19:2049–2062

Fairall C, Bradley E, Rogers D, Edson J, Young G (1996) Bulk parameterization of air–sea fluxes for tropical ocean-global atmosphere coupled-ocean atmosphere response experiment. J Geophys Res 101:3747–3764

Fairall C, Bradley E, Hare J, Grachev A, Edson J (2003) Bulk parameterization of air–sea fluxes: updates and verification for the CORE algorithm. J Clim 16:571–591

Fasullo J, Trenberth K (2008) The annual cycle of the energy budget: Meridional structures and transports. J Clim 21:2313–2325

Fekete B, Vorosmarty C, Grabs W (1999) An improved spatially distributed runoff data set based on observed river discharge and simulated water balance. Technical Report 22, Global Runoff Data Cent, 108 pp

Folland C, Karl T, Christy J, Clarke R, Gruza G, Jouzel J, Mann M, Oerlemans J, Salinger M, Wang S-W (2001) Observed climate variability and change. In: Houghton JT et al (eds) Climate change 2001: the scientific basis. intergovernmental panel on climate change. Contribution of Working Group I to the third assessment report, pp 99–181

Freilich M, Vanhoff B (2006) QuikSCAT vector wind accuracy through comparisons with National Data Buoy Center measurements. IEEE Trans Geosci Rem Sens 44:622–637. doi:10.1109/TGRS.2006.869928

French J, Drennan W, Zhang J, Black P (2007) Turbulent fluxes in the hurricane boundary layer. Part I: Momentum flux. J Atmos 64:1089–1102. doi:10.1175/JAS3887.1

Gates W (1992) AMIP: the atmospheric model intercomparison project. Bull Am Meteor Soc 73:1962–1970

Gent P (1991) The heat budget of the TOGA-COARE domain in an ocean model. J Geophys Res 96:3323–3330

Gibson J, Kallberg P, Uppala S, Hernandez A, Nomura A, Serrano E (1997) ECMWF re-analysis project, 1. ERA description, Project report series, ECMWF

Griffies S, Biastoch A, Boning C, Bryan F, Danabasoglu G, Chassignet E, England M, Gerdes R, Haak H, Hallberg R, Hazeleger W, Jungclaus J, Large W, Madex G, Samuels B, Scheinert M, Severijns C, Simmons H, Treguier A, Winton M, Yeager S, Yin J (2008) Coordinated ocean-ice reference experiments (COREs). Ocean Modell 11:59–74

Grist J, Josey S (2003) Inverse analysis adjustments of the SOC air–sea flux climatology using ocean heat transport constraints. J Clim 16:3274–3295

Hansen D, Poulain P-M (1996) Quality control and interpolations of WOCE-TOGA drifter data. J Atmos Oceanic Technol 13:900–909

Hellerman S, Rosenstein M (1983) Normal monthly wind stress over the World Ocean with error estimates. J Phys Oceanogr 13:1093–1104

Huffman G, Adler R, Arkin P, Chang A, Ferraro R, Gruber R, Janowiak J, McNab A, Rudolf B, Schneider U (1997) The global precipitation climatology project (GPCP) combined precipitation data set. Bull Am Meteor Soc 78:5–20

Hunke EC, Holland M (2007) Late winter generation of spiciness on subducted isopycnals. J Geophys Res 112:C04s14. doi: 10.1029/2009/2006JC003640

Hurrell J, Hack J, Shea D, Caron J, Rosinski J (2008) A new sea surface temperature and sea ice boundary data set for the community atmosphere model. J Clim (in press)

IPCC (2007) Climate change 2007: the physical science basis. Contribution of Working Group I to the fourth assessment report of the intergovernmental panel on climate change. In: Solomon S, Qin D, Manning M, Chen Z, Marquis M, Averyt K, Tignor M, Miller H (eds) Ocean circulation and climate. Cambridge University Press/Academic Press, London, p. 996

Isemer H-J, Willebrand J, Hasse L (1989) Fine adjustment of large scale air–sea energy flux parameterizations by direct estimates of ocean heat transport. J Clim 2:1173–1184

Jiang C, Cronin M, Kelly K, Thompson L (2005) Evaluation of a hybrid satellite and NWP based turbulent heat flux product using tropical atmosphere ocean (TAO) buoys. J Geophys Res 110. doi:10.1029/2004JC002824

Josey S, Kent E Taylor P (2002) Wind stress forcing of the ocean in the SOC climatology: comparisons with the NCEP-NCAR, ECMWF, UWM/COADS, and Hellerman and Rosenstein datasets. J Phys Oceanogr 32:1993–2019

Josey S, Kent E, Taylor P (1998) The Southampton Oceanography Centre (SOC) Ocean-Atmosphere Heat, Momentum and Freshwater flux Atlas. Technical report, Southampton Oceanography Centre Report No. 6 30pp

Josey S, Kent E, Taylor P (1999) New insights into the ocean heat budget closure problem from analysis of the SOC air–sea flux climatology. J Clim 12:2856–2868

Josey S, Kent E, Sinha B (2001) Can a state of the art atmospheric general circulation model reproduce recent NAO related variability at the air–sea interface?, Geophys Res Lett 28:4543–4546

Jost V, Bakan S, Fennig K (2002) HOAPS—a new satellite-derived freshwater flux climatology. Meteorol Zeitschrift 11:61–70

Kalnay E, Kanamitsu M, Kistler R, Collins W, Deaven D, Gandin L, Iredell M, Saha S, White G, Woollen J, Zhu Y, Chelliah M, Ebisuzaki W, Higgins W, Janowiak J, Mo K, Ropelewski C, Leetmaa A, Reynolds R, Jenne R (1996) The NCEP/NCAR 40-year reanalysis project. Bull Am Meteor Soc 77:437–471

Kubota M, Iwasaka N, Kizu S, Konda M, Kutsuwada K (2002) Japanese ocean flux data sets with use of remote sensing observations (J-OFURO). J Oceanogr 58:213–225

Large W (2006) Surface fluxes for practioners of global ocean data assimilattion. In: Chassignet E, Verron J (eds) Ocean weather and forecasting. Springer, Heidelberg, pp 229–270

Large W, Danabasoglu G (2006) Attribution and impacts of upper-ocean biases in CCSM3. J Clim 18:2325–2346

Large W, Nurser A (2001) Ocean surface water mass transformation. In: Siedler G, Church J, Gould J (eds) Ocean circulation and climate. International Geophysics Series, vol 77. Academic Press, New York, pp 317–336

Large W, Pond S (1981) Open ocean momentum flux measurements in moderate to strong winds. J Phys Oceanogr 11:324–336

Large W, Pond S (1982) Sensible and latent heat flux measurements over the ocean. J Phys Oceanogr 12:464–482

Large W, Yeager S (2004) Diurnal to decadal global forcing for ocean and seaice models: the data sets and climatologies. Technical Report TN-460+STR, NCAR, 105 pp

Large WG, Danabasoglu G, Doney SC, McWilliams JC (1997) Sensitivity to surface forcing and boundary layer mixing in a global ocean model: annual-mean climatology. J Phys Oceanogr 27:2418–2447

Levitus S, Antonov JI, Boyer TP, Stephens C (2000) Warming of the world ocean. Science 287:2225–2229

Lind R, Katsaros K (1986) Radiation measurements and model results from R/V Oceanographer during STREX 1980. J Geophys Res 91:13308–13314

MacDonald A, Wunsch C (1998) An estimate of global ocean circulation and heat fluxes. Nature 382:436–439

McPhaden M, Busalacchi A, Cheney R, Donguy J-R, Gage K, Halpern D, Ji M, Meyers PJG, Mitchum G, Niiler P, Picaut J, Reynolds R, Smith N, Takeuchi K (1998) The tropical ocean-global atmosphere observing system: a decade of progress. J Geophys Res 103:14169–14240

Naderi F, Freilich M, Long D (1991) Spaceborne radar measurements of wind vleocity over the ocean: an overview of the NSCAT scatterometer system. Proc IEEE 79:850–866

Payne R (1972) Albedo of the sea surface. J Atmos 29:959–970

Powell M, Vickery P, Reinhold T (2003) Reduced drag coefficients for high wind speeds is tropical cyclones. Nature 422:279–283

Rayner N, Parker D, Horton E, Folland C, Alexander L, Powell D (2003) Global analyses of SST, sea ice and night marine air temperature since the late nineteenth century. J Geophys Res 108. doi:10.1029/2002JD002670

Reynolds R, Rayner N, Smith T, Stokes D, Wang W (2002) An improved in situ and satellite SST analysis for climate. J Clim 15:1609–1625

Rigor I, Colony R, Martin S (2000) Variations in surface air temperature observations in the Arctic, 1979–1997. J Clim 13:896–914

Roske F (2006) A global heat and freshwater forcing data set for ocean models. Ocean Modell 11:235–297

Schacher G, Davidson K, Houlihan T, Fairall C (1981) Measurements of the rate of dissipation of turbulent kinetic energy over the ocean. Boundary Layer Meteorol 20:321–330

Serreze M, Hurst C (2000) Representation of mean Arctic precipitation from NCEP-NCAR and ERA reanalyses. J Clim 13:182–201

Servain J, Busalacchi A, McPhaden M, Moura A-D, Reverdin G, Vianna M, Zebiak S (1998) A pilot research moored array in the tropical Atlantic (PIRATA). Bull Am Meteor Soc 79:2019–2031

Smith S (1988) Coefficients for sea surface wind stress, heat flux, and wind profiles as functions of wind speed and temperature. J Geophys Res 93:15467–15472

Smith SR, Legler DM, Verzone KV (2001) Quantifying uncertainties in NCEP reanalyses using high-quality research vessel observations. J Clim 14:4062–4072

Spencer RW (1993) Global oceanic precipitation from the MSU during 1979–91 and comparisons to other climatologies. J Clim 6:1301–1326

Stammer D, Wunsch C, Giering R, Ekert C, Heimbach P, Marotzke J, Adcroft A, Hill C, Marshall J (2002) The global ocean circulation during 1992–1997, estimated from ocean observations and a general circulation model. J Geophys Res 107:3118. doi:10.1029/2001JC000888

Stammer D, Ueyoshi K, Large W, Josey S, Wunsch C (2004) Estimating air–sea fluxes of heat, freshwater and momentum through global ocean data assimilation. J Geophys Res 109. doi:10.1029/2003JC002082

Taylor (ed.), P. 2000 Final report of the joint WCRP/SCOR Working Group on air–sea fluxes: intercomparison and validation of ocean–atmosphere energy flux fields, WCRP-112, WMO/TD-No.1036, World Climate Research Programme, 303 pp

Trenberth K, Caron J (2001) Estimates of meridional atmosphere and ocean heat transports. J Clim 14:3433–3443

Uppala S, co authors (2005) The ERA-40 re-analysis. Q J Roy Meteor Soc 131:2961–3012. doi:101256/qj.04.176

Visbeck M, Chassignet E, Curry R, Delworth T (2003) The ocean's response to North Atlantic variability. The North Atlantic oscillation, In: Hurrell J, Kushnir Y, Ottersen G, Visbeck M (eds) Geophysical monograph, vol 134. American Geophysical Union, pp 113–145

Wang W, McPhaden MJ (2001) What is the mean seasonal cycle of surface heat flux in the equatorial Pacific?, J Geophys Res 106:837–857

Wentz F, Ricciardulli L, Mears C (2007) How much more rain will global warming bring?. Science 317:233–235

Wijffels S (2001) Ocean transport of freshwater, ocean circulation and climate. In: Siedler G, Church J, Gould J (eds) International geophysics series, vol 77. Academic Press, New York, pp 475–488

Wittenburg A, Rossati A, Lau N, Ploshay J (2006) GFDL's CM2 global coupled climate models. Part III: Tropical Pacific climate and ENSO. J Clim 19:698–722

Xie P, Arkin PA (1996) analyses of global monthly precipitation using gauge observations, satellite estimates, and numerical model predictions. J Clim 9:840–858

Yang D (1999) An improved precipitation climatology for the Arctic Ocean. Geophys Res Lett 26:1625–1628

Yeager S, Large W (2004) Late winter generation of spiciness on subducted isopycnals. J Phys Oceanogr 34:1528–1547

Yeager S, Large W, Hack J, Shields C (2005) The low resolution CCSM3. J Clim 18:2545–2566

Yu L, Weller R (2007) Objectively analyzed air–sea heat fluxes for the global ice-free oceans (1981–2005). Bull Am Meteor Soc 88. doi:10.1175/BAMS-88-4-527

Yu L, Weller R, Sun B (2004) Improving latent and sensible heat flux estimates for the Atlantic Ocean (1988–1999) by a synthesis approach. J Clim 17:373–393

Zhang Y, Rossow W, Lacis A, Oinas V, Mishchenko M (2004) Calculation of radiative flux profiles from the surface to top-of-atmosphere based on ISCCP and other global data sets: refinements of the radiative transfer model and input data. J Geophys Res 109. doi:10.1029/2003JD004457